ScienceDirect

Modern Cartography Series

Volume 12, 2024, Pages 261-297

Chapter 11 - Agricultural drought monitoring using Google Earth Engine: a study of Paschim Medinipur district, West Bengal

Pulakesh Pradhan, Sribas Patra

https://doi.org/10.1016/B978-0-443-23890-1.00011-6

Get rights and content

Pulakesh Pradhan

pulakeshpradhan@ravenshawuniversity.ac.in

pulakesh.mid@gmail.com

https://orcid.org/0000-0003-3103-3617

PhD Scholar, Departmentof Geography, Ravenshaw University, Odisha, India

Sribas Patra

sribaspatra2013@gmail.com

https://orcid.org/0000-0001-7289-4080

PhD Scholar, Departmentof Geography, Ravenshaw University, Odisha, India

CHAPTER

11 Agricultural drought monitoring using Google Earth Engine: a study of Paschim Medinipur district, West Bengal

Pulakesh Pradhan and Sribas Patra
Department of Geography, Ravenshaw University, Cuttack, Odisha, India

11.1 Introduction

Drought is a natural climatological phenomenon (Sreekesh, Kaur, & Naik, 2019) characterized by the deficiency in the precipitation (Kogan, 1995; Mckee, Doesken, & Kleist, 1993; Sreekesh et al., 2019) and abnormally dry weather conditions (Alahacoon, Edirisinghe, & Ranagalage, 2021; Eklund, Mohr, & Dinc, 2024; Kogan, 1995) with water scarcity (Senamaw, Addisu, & Suryabhagavan, 2021). Agricultural drought refers to a period of insufficient soil moisture for crop growth (Ji & Peters, 2003; Roy, Hazra, & Chanda, 2023; Senapati, Raha, Das, & Gayen, 2021) that negatively affects crop production (Eklund et al., 2024; Mishra & Singh, 2010; Pan et al., 2023). There are several other driving factors that lead to the agricultural drought like excessive evapotranspiration due to rising temperatures (Anderson, Norman, Mecikalski, Otkin, & Kustas, 2007; Vicente-Serrano, Beguería, & López-Moreno, 2010), climatic variabilities and changes in climatic patters (Senapati et al., 2021), deforestation and degradation (Tran et al., 2023), weakening of Indian monsoon (Chattopadhyay, Malathi, Tidke, Attri, & Ray, 2020), global warming (Cai et al., 2024), poor water management practices (Alahacoon et al., 2021), and so forth. Identifying agricultural drought in a timely and accurate manner is critical for assessing crop conditions, managing irrigation water, and mitigating farming risks (Moran, Clarke, Inoue, & Vidal, 1994). It is helpful for developing agricultural water strategies (Zhang, Huang, & Li, 2024), ensuring food security (Becker-Reshef, Vermote, Lindeman, & Justice, 2010), and livelihood (Seshasai et al., 2016), essential for selecting appropriate drought management practices for farmers, government bodies, media, and insurance companies (Sreekesh et al., 2019). Agricultural drought monitoring through remote sensing and climate datasets (Cai et al., 2023; Mistry & Suryanarayana, 2023) has become an important approach for assessing crop–climate relationships

Applications of Geospatial Technology and Modeling for River Basin Management.
DOI: https://doi.org/10.1016/B978-0-443-23890-1.00011-6

(Alahacoon et al., 2021; Ji & Peters, 2003; Kogan, 1995; Mishra & Singh, 2010; Thavorntam & Tantemsapya, 2013). Multiple studies have used vegetation indices like Normalized Difference Vegetation Index (NDVI), Temperature Condition Index (TCI), and Vegetation Condition Index (VCI) (Alahacoon et al., 2021; Thavorntam & Tantemsapya, 2013), drought indices like Standardized Precipitation Index (SPI), Palmer Drought Severity Index (PDSI), and so forth (Bashit, Ristianti, & Ulfiana, 2022), and climatic indices like Normalized Difference Drought Index and Rainfall Anomaly Index (Alahacoon et al., 2021) to access the agricultural drought patterns and crop responses (Chattopadhyay et al., 2020; Hasan & Abdullah, 2022).

11.1.1 Drought indices

For the drought monitoring, precipitation-based SPI (Mckee et al., 1993), PDSI incorporating moisture supply and demand, and Standardized Precipitation Evapotranspiration Index (SPEI) combining precipitation and potential evapotranspiration (PET) (Vicente-Serrano et al., 2010) are widely utilized. Satellite-derived actual evapotranspiration (AET) provides direct crop water use estimates (González & Valdés, 2006). Moisture stress is quantified by the Evaporative Stress Index (Anderson et al., 2007), evaporative fraction, and Crop Water Deficit Index. Soil moisture downscaling techniques also improve drought (Sreekesh et al., 2019; Zhang et al., 2024).

11.1.2 Vegetation indices

Vegetation indices from satellite optical and thermal sensors, particularly NDVI, have been widely used to monitor agricultural drought impacts on crop condition and yields (Amin et al., 2020; Becker-Reshef et al., 2010; Zhang et al., 2022). Decreasing crop NDVI during key phenological stages signals agricultural drought onset and stress (Ji & Peters, 2003; Kogan, 1995). VCI and TCI incorporate historical NDVI and land surface temperature (LST) for agricultural drought detection (Dong, Li, Yuan, You, & Chen, 2017; Kogan, 1995). Combining NDVI and LST, the Vegetation Health Index (VHI) indicates overall crop status (Geng, Zhang, Gu, He, & Zheng, 2024; Kogan, 1995; Possega, Ojeda, & Gámiz-Fortis, 2023). Microwave indices including Vegetation Optical Depth and Vegetation Water Content provide complementary information on vegetation and soil moisture dynamics (Liu et al., 2011; Sims, Niyogi, & Raman, 2002). Radiometric indices such as Normalized Multiband Drought Index are also applied for agricultural drought monitoring (Wang et al., 2022).

11.1.3 Agricultural drought studies

Senapati et al. (2021) carried out a detailed assessment of the agricultural drought susceptibility in the Purulia and Bankura districts, which are located in the

western part of West Bengal. Using MODIS and SAR data (Kloos, Yuan, Castelli, & Menzel, 2021; Roy et al., 2023), the monthly agricultural droughts were examined, which occurred in the red and lateritic zones of West Bengal throughout the monsoon seasons. They determined that the severe to extreme drought conditions that resulted in crop failures occurred in three acute drought years: 2005, 2010, and 2015. Using a variety of remote sensing and GIS tools (Kaur, Rishi, & Chaudhary, 2022), another study attempted to determine the spatiotemporal variance of agricultural drought. In India, Chattopadhyay et al. (2020) used a composite drought index to track agricultural drought. The survey was conducted in five Indian states, Andhra Pradesh, Chhattisgarh, Haryana, Maharashtra, and Telangana, over the course of three consecutive years: 2014, 2015, and 2016. A different study examined the nation's current operational and research projects, as well as methods for assessing droughts. The spatiotemporal patterns of agricultural drought in West Bengal, India, are better understood thanks to these studies.

11.1.4 Approach in the present study

This study utilizes several key vegetation and drought indices that were derived from optical, thermal, and microwave satellite data to analyze agricultural drought patterns and crop responses over a 20-year period in the major farming region. Climate-based drought indices such as the SPI (Mckee et al., 1993) and the SPEI (Vicente-Serrano et al., 2010) can identify shortfalls in precipitation when compared to average seasonal norms (Kumar & Chu, 2024; Liu et al., 2016). These indicate drought caused by lack of rainfall recharge for soils. The TerraClimate Dataset is a comprehensive resource that provides several key indicators for analyzing drought conditions. These include AET, which measures the actual transfer of water from the land to the atmosphere, offering insights into the water cycle and plant growth potential. The climate water deficit measures the difference between potential and AET, serving as an indicator of environmental water stress. Soil moisture is another critical indicator, reflecting the water available in the soil for plant uptake, with changes in its levels often signaling the onset of drought conditions. Additionally, the dataset includes minimum and maximum temperature, as temperature extremes can intensify drought conditions by increasing evaporation rates and water demand. Lastly, the PDSI provides a standardized measure of drought severity, incorporating both precipitation and temperature. Together, these indicators offer a holistic view of drought conditions, enabling more accurate predictions and facilitating effective water resource management strategies (Tanarhte, De Vries, Zittis, & Chfadi, 2024). Changes in vegetation during the pre- and postmonsoon period were quantified by analyzing satellite vegetation indices like NDVI, VCI, and VHI. Climatic influence was analyzed and qualified through LST and TCI, and the water condition was analyzed through the NDWI (Fig. 11.1).

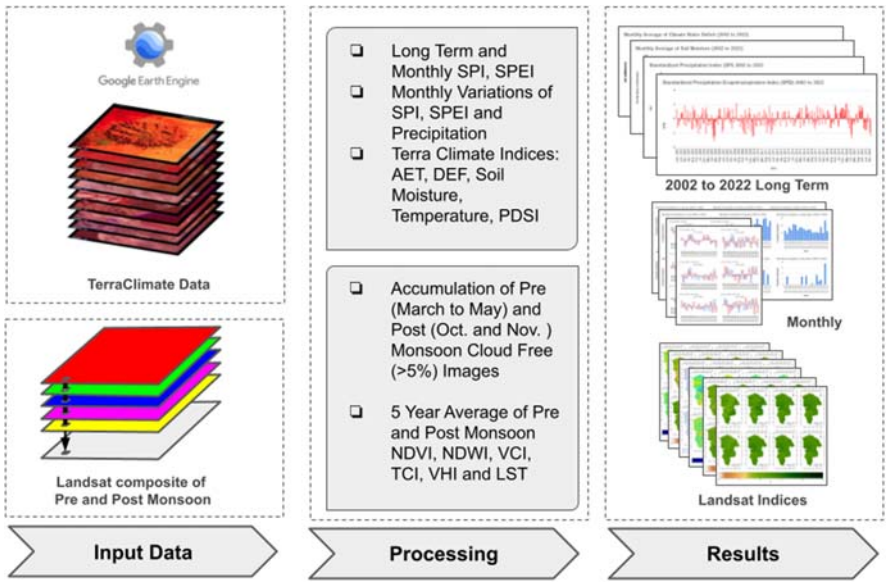

FIGURE 11.1

Methodology chart of the study.

11.2 Study area

The study area, Paschim Medinipur district, is located in the state of West Bengal, India (Fig. 11.2). The district is located in the southern part of West Bengal adjacent to the Bay of Bengal. It is bounded by the Purba Medinipur district to the east, Jhargram district to the west, Bankura and Purulia districts to the north, and the state of Odisha to the south. Paschim Medinipur has a subtropical climate influenced by the southwest monsoon. Average annual rainfall is around 1400 mm, of which 80% is received during the summer monsoon months of June to September (Jana, Sit, & Chanda, 2021; Panda, Upadhyay, Jha, & Sharma, 2020). Temperatures range from 12°C in winter to over 40°C prior to monsoon onset, with high humidity levels. The primary river systems are the Kangsabati, Rasulpur, and Haldi, which are tributaries of the Hooghly River. Canals from these rivers provide irrigation to some areas, although much of the district depends on rain-fed agriculture. Paschim Medinipur is predominantly rural and agrarian, with over 80% of the population engaged in agriculture and related activities. Rice is the major crop during the kharif (summer monsoon) season. Oil seeds such as groundnut and sesame, pulses like arhar, and vegetables including okra, brinjal, and cucurbits are also cultivated across the district (Sen & Bhakat, 2021). The main rabi (winter) crops are sunflower, mustard, potatoes, and vegetables. Forested areas are mainly found in the western region.

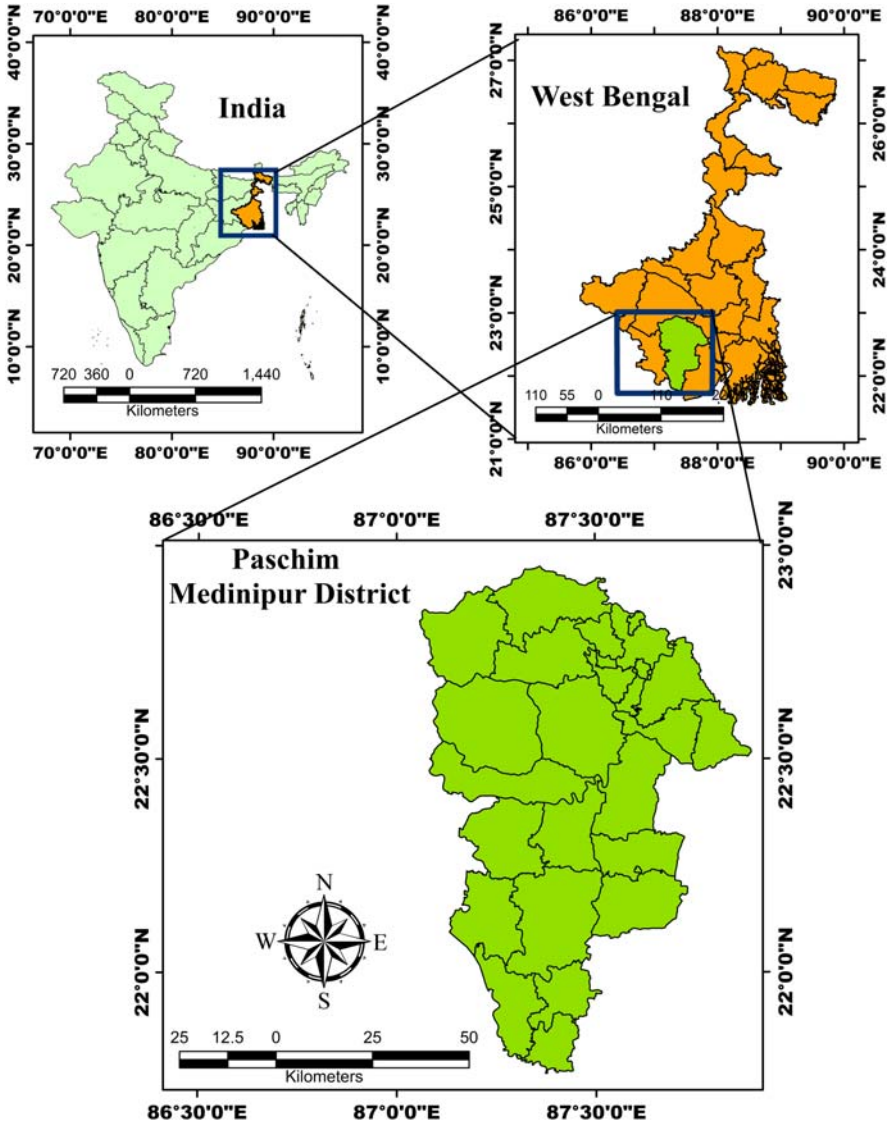

FIGURE 11.2

Location map of the study area. Map lines delineate study areas and do not necessarily depict accepted national boundaries.

11.2.1 Drought vulnerability

High rainfall variability coupled with limited irrigation infrastructure leaves the region prone to frequent agricultural droughts. Kharif rice is highly vulnerable to

monsoon rainfall deficits. Recurrent droughts lead to low farm incomes, food insecurity, indebtedness, and distress migration. Integrating satellite and climate datasets can delineate drought patterns, associated crop responses, and vulnerable zones to inform adaptation strategies (Li et al., 2024; Xiao et al., 2024).

11.3 Datasets

TerraClimate and Landsat series datasets were used in this investigation (Ghaleb et al., 2015; Hazaymeh & Hassan, 2016). Landsat data were gathered seasonally, particularly before and after the monsoon. Premonsoon months were taken from March to May, while postmonsoon months were taken from October to November. Datasets with 5-year intervals were gathered from 2002 to 2022. The datasets were obtained from the US Geological Survey via the Google Earth Engine (GEE) platform (Gorelick et al., 2017). The Landsat datasets were collected with a 5% cloud cover. This study employed a total of 83 Landsat 5 and 118 Landsat 8 images. TerraClimate datasets were also gathered from 2002 to 2022 using the GEE platform. Monthly average precipitation data, as well as AET, climate water deficit, soil moisture, minimum and maximum temperature, and the PDSI, were collected (Table 11.1). The images were processed in the GEE platform.

11.3.1 Methodology

In the present study, multiple indices were used for determination of agriculture drought in Paschim Medinipur district of West Bengal. This study made use of

Table 11.1 Different data sources for the study.

Datasets	Name of the data	Duration	Months	Numbers of images
Terra-climate datasets	Precipitation	2002–22	Jan–Dec	4638.3 m spatial resolution
	AET	2002–22	Jan–Dec	
	Climate water deficit	2002–22	Jan–Dec	
	Soil moisture	2002–22	Jan–Dec	
	Minimum and maximum temperature	2002–22	Jan–Dec	
	PDSI	2002–22	Jan–Dec	
Satellite datasets	Landsat 5 TM	2003–07	March–May and Oct–Nov	47
		2008–12		36
	Landsat 8 TIRS/OLI	2013–17		58
		2018–22		60

the following indices: LST, NDVI, Normalized Difference Water Index (NDWI), SPI, SPEI, VCI, TCI, VHI, and so on. The study's whole methodology is displayed in Fig. 11.4.

11.3.1.1 Standardized Precipitation Index

The SPI is one of the drought indices that the WMO has approved for use globally, which was put forth by Mckee et al. (1993). The SPI is a multiscalar index that solely relies on precipitation. This method gained a lot of acceptance and is now extensively used to research drought for applications in various sectors because it is straightforward and takes various timescales into account (Fig. 11.3).

Eqs. 11.1–11.6 represent the procedure of calculating the SPI. For the precipitation value of x over a given period, the distribution of probability density function of Γ is as follows:

$$F(x) = \frac{1}{\beta^{\gamma}\Gamma(\gamma_0)} x^{\gamma-1} e^{-x/\beta}, x > 0 \tag{11.1}$$

where β and y are scale and shape parameters of the distribution function (Γ), respectively.

The probability of all precipitation events (x) that are smaller than the x_0 for a given year is:

$$F(x < x_0) = \int_0^{\infty} f(x)dx \tag{11.2}$$

and

$$F(x = 0) = m/n \tag{11.3}$$

where m is the number of days with no precipitation ($x = 0$) and n is the total number of days.

The normal standardizing of the Γ probability function is done through substitution of the result of probability value in the standardized normal distribution function:

$$f(x < x_0) = \frac{1}{\sqrt{2\pi}} \int_0^{\infty} e^{-x^2/2} dx \tag{11.4}$$

By solving the abovementioned equation, the SPI would be as follows:

$$\text{SPI} = S \frac{t - (c_2 t + c_1) + c_0}{[(d_3 + d_2)t + d_1]t + 1} \tag{11.5}$$

where

$$t = \sqrt{\ln \frac{1}{F^2}} \tag{11.6}$$

```
// SPI
function getGammaDistParams(col){
  // Shape/rate-based gamma distribution as defined in Wikipedia: Get the gamma distribution parameters. Input = the collection
  var col_no0 = col.map(function(img){return img.updateMask(img.neq(0))});// Masks pixels with 0 values
  var N=col_no0.count(); // Reduces an image collection by calculating the number of images with a valid mask at each pixel across the stack of all matching bands. Bands
  var sum_log=col_no0.map(function(img){return img.log()}).sum();
  var A = (col_no0.mean().log()).subtract(sum_log.divide(N));
  var iA4 = ee.Image.constant(4).multiply(A);
  var i1 = ee.Image.constant(1);
  var i3 = ee.Image.constant(3);
  var alpha = (i1.divide(iA4)).multiply(i1.add((i1.add(iA4.divide(i3))).sqrt()));
  var beta = col_no0.mean().divide(alpha);
  var param = alpha.addBands(beta).select([0,1],["alpha","beta"]);
  return param;
}
// Get q, the probability of zeros. Input =  the collection
function getQ(col){ // Get the probability of a zero CHECK that the probability is on Pi and not Pr
  var PiNot0 = col.map(function(img){return img.updateMask(img.neq(0))}); // Mask all null values
  var N = col.count();
  var m = N.subtract(PiNot0.count()); // calculating the number of images with 0 at each pixel
  var q = ee.Image(m.divide(N));
  return q.select([0], ['q']);
}
function getHxSPI(img){
   var i1 = ee.Image.constant(1);
   var coef = img.divide(beta);
   var Gx = ee.Image(alpha.gammainc(coef)); // CDF for shape/scale based gamma functin. Definition found in Wikipedia
   // Note: gammainc(x,a) is the regularized lower incomplete gamma function, which is equal to the lower incomplete gamma divided by gamma(x). So, in your particular cas
   var Hx = Gx.addBands(q.add((i1.subtract(q)).multiply(Gx))).select([0, 1], ['Gx', 'Hx']);
    //Calculate SPI
    var c0 = ee.Image.constant(2.515517);
    var c1 = ee.Image.constant(0.802853);
    var c2 = ee.Image.constant(0.010328);
    var d1 = ee.Image.constant(1.432788);
    var d2 = ee.Image.constant(0.189269);
    var d3 = ee.Image.constant(0.001308);

    var in1 = ee.Image.constant(-1);
    var t1 = ee.Image(((i1.divide(Hx.pow(2))).log()).pow(0.5)).select([0], ["t1"]);
    var t2 = ee.Image(((i1.divide(i1.subtract(Hx)).pow(2)).log()).pow(0.5)).select([0], ["t2"]);
    var t = t1.where(Hx.select('Hx').gt(.5), t2).select([0], ['t']);
    var div = t.subtract((c0.add(c1.multiply(t)).add(c2.multiply(t.pow(2))))).divide(i1.add(d1.multiply(t)).add(d2.multiply(t.pow(2))).add(d3.multiply(t.pow(3))));
    var SPI = in1.multiply(div).where(Hx.select('Hx').lte(.5), div).select([0], ['SPI']);

    return Hx.addBands(SPI).select([0, 1, 2],['Gx', 'Hx', 'SPI'])
     .set({'time': ee.Date.fromYMD(img.get('year'), img.get('month'), 1)});//,
  }
// *** getLogLogisticDistParam: Obtain parameters of the log logistic distribution
// Input:  the collection holding Di = Pi-ETi data over the chosen window
function getLogLogisticDistParam(col){
var N = col.count();
// Calculate probability-weighted moments
// Convert the entire collection to an array-based image, and arraySort it
var array = col.toArray();
var DiSorted = array.arraySlice(1, 0).arraySort().arrayProject([0]);
/// START CHANGE///
var i = ee.Image.constant(ee.Array(ee.List.sequence(1, col.size())));
/// END CHANGE///
var Fi = ((i.subtract(ee.Image.constant(.35))).divide(N));
var FiDi = DiSorted.addBands(Fi).select([0,1], ['DiSorted', 'Fi']);
var pwm0 = ee.Image(((ee.Image.constant(1).subtract(Fi)).pow(0).multiply(DiSorted)))
    .arrayAccum(0).arraySlice(0, N.subtract(1)).divide(N);
var pwm1 = ee.Image(((ee.Image.constant(1).subtract(Fi)).pow(1).multiply(DiSorted)))
    .arrayAccum(0).arraySlice(0, N.subtract(1)).divide(N);
var pwm2 = ee.Image(((ee.Image.constant(1).subtract(Fi)).pow(2).multiply(DiSorted)))
    .arrayAccum(0).arraySlice(0, N.subtract(1)).divide(N);
var pwm = pwm0.addBands(pwm1).addBands(pwm2);
// Calculate alpha, beta, gamma
var i1 = ee.Image.constant(1);
var i2 = ee.Image.constant(2);
var i6 = ee.Image.constant(6);
var beta = (i2.multiply(pwm1).subtract(pwm0))
      .divide((i6.multiply(pwm1)).subtract(pwm0).subtract(i6.multiply(pwm2)));
var gamF1 = (i1.add(i1.divide(beta))).gamma();
var gamF2 = (i1.subtract(i1.divide(beta))).gamma();
var alpha = ((pwm0.subtract(i2.multiply(pwm1))).multiply(beta)) // // Error in the Serano paper (multiply(beta) and NOT divide(beta); according to
      .divide((gamF1).multiply(gamF2));
var gamm = pwm0.subtract((alpha).multiply(gamF1).multiply(gamF2)); // Error in the Serano paper according to the source paper Singh 1993
var param = beta.addBands(alpha).addBands(gamm).select([0,1,2],['beta','alpha','gamma']);
return param;
}
//*** getFxSPEI: obtain Fx and SPEI
/// START CHANGE ///
function getFxSPEI(img){
  var i1 = ee.Image.constant(1);
  var in1 = ee.Image.constant(-1);
  var in2 = ee.Image.constant(-2);

  var Fx = (i1.add((alpha.divide(img.subtract(gamm))).pow(beta))).pow(-1).arrayFlatten([['0']]);
  var Px = i1.subtract(Fx);
  var W1 = (in2.multiply((Px).log())).sqrt();
  var W2 = (in2.multiply((i1.subtract(Px)).log())).sqrt();

  var W = W1.where(Px.gt(ee.Image.constant(.5)), W2);
  var C0 = ee.Image.constant(2.515517);
  var C1 = ee.Image.constant(0.802853);
  var C2 = ee.Image.constant(0.010328);
  var d1 = ee.Image.constant(1.432788);
  var d2 = ee.Image.constant(0.189269);
  var d3 = ee.Image.constant(0.001308);

  var SPEI00 = W.subtract((C0.add(C1.multiply(W)).add(C2.multiply(W.pow(2))))
               .divide(i1.add(d1.multiply(W)).add(d2.multiply(W.pow(2))).add(d3.multiply(W.pow(3)))));

  var SPEI0 = SPEI00.where(Px.gt(ee.Image.constant(.5)), in1.multiply(SPEI00));

  var SPEI = Fx.addBands(SPEI0).select([0,1], ['Fx', 'SPEI'])
        .set({'time': ee.Date.fromYMD(img.get('year'), img.get('month'), 1)});
  return SPEI;//
}
```

FIGURE 11.3

Google Earth Engine script for Standardized Precipitation Index and Standardized Precipitation Evapotranspiration Index.

$$c_0 = 2.515517; c_1 = 0.802853; c_2 = 0.010328$$
$$d_1 = 1.432788; d_2 = 0.189269; d_3 = 0.001308$$

c_0, c_1, c_2, d_1, d_2, and d_3 are constant parameters of SPI. The sign of the SPI is identified by coefficient S that is based on the value of F. For $F > 0.5$, the S equals 1 and for $F \leq 0.5$, the S equals -1.

11.3.1.2 Standardized Precipitation Evapotranspiration Index

The SPEI, which added the PET as an input, was proposed by Vicente-Serrano et al. (2010), based on the SPI method with a basic climatic water balance. PDSI's sensitivity to atmospheric water demand and SPI's multiscale characteristic are both present in SPEI (Fig. 11.3). Compared to other approaches, it is more favorable because of these benefits and its relative simplicity. According to Vicente-Serrano et al. (2010), the SPEI computation process is shown in Eqs. 11.7−11.14. To estimate the PET, a variety of techniques are available (such as Thornthwaite approach, Penman−Monteith method, Hargreaves method, etc.). The following would be the moisture-deficit for the month after calculating the PET using any of the different methods:

$$D_i = P_i - \mathrm{PET}_i \tag{11.7}$$

The standardization is followed by selection of the probability density function of a three-parameter loglogistic distributed variable as follows:

$$f(x) = \frac{\beta}{\alpha}\left(\frac{x-\gamma}{\alpha}\right)^{\beta-1}\left(1+\left(\frac{x-\gamma}{\alpha}\right)^{\beta}\right)^{-2} \tag{11.8}$$

in which α, β, and y are scale, shape, and origin parameters, respectively; with D values in the range of $y > D < \infty$. These parameters are obtained through Eqs. 11.9−11.11:

$$\beta = \frac{2w_1 - w_0}{6w_1 - w_0 - 6w_2} \tag{11.9}$$

$$\alpha = \frac{(w_0 - 2w_1)\beta}{\Gamma(1 + 1/\beta)\Gamma(1 - 1/\beta)} \tag{11.10}$$

$$\gamma = w_0 - \alpha\Gamma\left(1 + \frac{1}{\beta}\right)\Gamma\left(1 - \frac{1}{\beta}\right) \tag{11.11}$$

where $\Gamma(\beta)$ is the gamma function of β.

The probability density function of D based on the given distribution of three-parameter log-logistic is as follows:

$$F(x) = \left[a + \left(\frac{\propto}{x-\gamma}\right)^{\beta}\right]^{-1} \tag{11.12}$$

Then, the SPEI is calculated as the standardized values of $F(x)$ as follows:

$$\mathrm{SPEI} = W - \frac{C_0 + C_1 W + C_2 W^2}{1 + d_1 W + d_2 W^2 + d_3 W^3} \tag{11.13}$$

Given P is the probability of exceeding a given D value ($P = 1 - F(x)$), for $P \leq 0.5$, the W is:

$$W = -2\ln(P) \tag{11.14}$$

And, if $P > 0.5$, then P is replaced by $1 - P$ and the sign of the resultant *SPEI* is reversed.

Six constant parameters of the SPEI equation are as follows:

$$c_0 = 2.515517; c_1 = 0.802853; c_2 = 0.010328$$
$$d_1 = 1.432788; d_2 = 0.189269; d_3 = 0.001308$$

11.3.1.3 Normalized Difference Vegetation Index

NDVI as a standard method for assessing the healthy and green vegetation by calculating the difference between near-infrared and red light (Senamaw et al., 2021; Sruthi, Mohammed Aslam, 2015), as shown in Eq. 11.15.

$$\mathrm{NDVI} = \frac{(\mathrm{NIR} - R)}{(\mathrm{NIR} + R)} \tag{11.15}$$

where NIR = near infrared band, R = Red band

According to Thavorntam and Tantemsapya (2013), the NDVI is a potent indicator for tracking the amount of vegetation covering large regions as well as for identifying the frequency and duration of droughts. It gives an indication of the quantity and health of plants at the surface of the ground. The amount of photosynthetic activity in the observed vegetation is correlated with the NDVI magnitude. Higher NDVI scores often correspond to higher levels of vegetation vigor.

11.3.1.4 Vegetation Condition Index

The VCI exhibited the changeable moisture conditions and indicated vegetation dynamics. Maximum levels of this measure show healthy, undisturbed vegetation. The index is very useful for measuring vegetation stress and examining how plant responds (Dutta et al., 2015) Eq. 11.16.

$$\mathrm{VCI} = \frac{100 \times (\mathrm{NDVI} - \mathrm{NDVI}_{\mathrm{min}})}{\mathrm{NDVI}_{\mathrm{max}} - \mathrm{NDVI}_{\mathrm{min}}} \tag{11.16}$$

The proportion of the VCI value is expressed in terms of 1−100. While readings ranging from 50% to 35% indicate a drought state and values below 35% indicate a severe drought condition, the range between 50% and 100% indicates above average vegetation condition.

11.3.1.5 Temperature Condition Index

TCI is used to assess the stress that high temperatures and heavy moisture have on vegetation. It is calculated by Eq. 11.17 (Alahacoon et al., 2021)

$$\mathrm{TCI} = \frac{100 \times \mathrm{LST}_{\max} - \mathrm{LST}}{\mathrm{LST}_{\max} - \mathrm{LST}_{\min}} \tag{11.17}$$

A TCI rating of 50% denotes normal conditions or the absence of drought. TCI levels below 50% indicate different degrees of drought severity, whereas TCI values above 50% reflect the ideal/above normal situation.

11.3.1.6 Vegetation Health Index

Analysis of the drought VHI is one of the important remote sensing indices. Both the NDVI and the LST can be used to calculate the VHI by Eq. 11.18 (Alahacoon et al., 2021).

$$\mathrm{VHI} = (0.5 \times \mathrm{VCI}) + (0.5 \times \mathrm{TCI}) \tag{11.18}$$

The VHI value is distributed between 0 and 100. Drought is indicated by low VHI values, whereas robust vegetation is indicated by high values.

11.3.1.7 Normalized Difference Water Index

When assessing drought, NDWI with SWIR can be used in addition to NDVI, especially early in the drought season. It is calculated following Eq. 11.19

$$\mathrm{NDVI} = \frac{(\mathrm{NIR} - \mathrm{SWIR})}{(\mathrm{NIR} + \mathrm{SWIR})} \tag{11.19}$$

where NIR is the near-infrared band, and SWIR is the short wave infrared band of the satellite imageries.

11.3.1.8 Land surface temperature

The LST of the Paschim Medinipur district was determined using Landsat TM 5 imagery for the years 2002 to 2012 and Landsat 8 OLI (Operational Land Imager) for the years 2013 to 2022 with less than 5% cloud cover. While Landsat 8 OLI imagery includes 11 bands, including bands 10 and 11, which are thermal bands (Eqs. 11.20–11.25), Landsat TM 5 imagery only provides 7 bands. The steps involved in converting digital values into spectral radiance for temperature calculation from TM and OLI images are as follows:

Step 1: Landsat TM 5 band 6 digital values to spectral radiances conversion.

The following formula was used to convert band 6 digital values into radiance values ($L\lambda$) (Ara, Alif, & Islam, 2021)

$$L\lambda = \frac{\mathrm{LMAX}\lambda - \mathrm{LMIN}\lambda}{\mathrm{QCALMAX} - \mathrm{QCALMIN}} \times (\mathrm{QCAL} - \mathrm{QCALMIN}) + \mathrm{LMIN}\lambda \tag{11.20}$$

Here, $L\lambda$ is the atmospherically corrected cell value as the radiance, QCAL is the digital image value, LMINλ is the spectral radiance scaled to QCALMIN, LMAXλ

is the spectral radiance scaled to QCALMAX, and QCALMIN is the minimum quantization calibration. The radiance pixel value (usually 1) and QCALMAX are the maximum values of quantized calibrated pixels (usually 255). Landsat 8 OLI spectral radiances were converted from band 10 and 11 digital data.

The following formula was used to convert the Landsat OLI band 10 and 11 digital data.

$$L\lambda = \mathrm{ML} \times \mathrm{QCAL} + \mathrm{AL} \tag{11.21}$$

where $L\lambda$ is the spectral radiance at the top of the atmosphere, ML denotes the radiance multiband X, AL denotes the radiance add band X, QCAL denotes the quantized and calibrated standard product pixel value, and X denotes the band number. The band-specific multiplicative rescaling factor ML and the band-specific additive rescaling factor AL are obtained from the metadata file (MTL file).

Step 2: At-satellite brightness spectral radiance temperature conversion—emissivity modifications were added to radiant temperature based on the land cover nature following Ara et al. (2021).

$$T = \frac{K_2}{Ln\left(\frac{\kappa_1}{L\lambda} + 1\right)} - 273 \cdot 15 \tag{11.22}$$

where T is the at-satellite brightness temperature in Kelvin (K), $L\lambda$ is the at-satellite radiance in W/(m^2 sr μm), and K_1 and K_2 are the thermal calibration constants in W/(m^2 sr μm), respectively. For Landsat-5 TM, $K_1 = 607.76$ and $K_2 = 1260.56$ for band 6, and for Landsat 8 OLI, K_1 for band 10 and 11 is 774.8853 and 480.8883 respectively, and K_2 for band 10 and 11 is 1321.0789 and 1201.1442, respectively. The metadata file provided the values for K_2 and K_1. For a better understanding, the thermal constant values for Landsat TM and Landsat OLI are converted from K to °C using the equation 0°C = 273.15K.

Step 3: Emissions from the ground surface are measured (E).

The temperature values derived above are compared to a black body. As a result, spectral emissivity (E) adjustments are required. These can be done according to the land cover type or by calculating the emissivity values for each pixel from the proportion of vegetation (P_V) data (Shahfahad et al., 2021).

$$E = 0.004^* P_V + 0.986 \tag{11.23}$$

where the P_V can be calculated as:

$$P_V = \left\{\frac{(\mathrm{NDVI}_{\max} - \mathrm{NDVI}_{\min})}{(\mathrm{NDVI}_{\max} - \mathrm{NDVI}_{\min})}\right\}^2 \tag{11.24}$$

Step 4: LST is calculated using the equation below (Govind & Ramesh, 2020).

$$\frac{\mathrm{BT}}{1} + W^* \left(\frac{\mathrm{BT}}{P}\right)^* Ln(E) \tag{11.25}$$

where BT is the brightness temperature at the satellite, W is the wavelength of emitted radiance, $P = h^*c/s$ (1.438 10−2 m K), h is the Planck's constant (6.626 10−34 Js), s is the Boltzmann constant (1.38 10−23 J/K), and the light velocity is 2.998 10 8 m/s.

11.4 Results and discussion

The entire analysis has been segmented in three parts; the first section focuses on analysis of precipitation with SPI and SPEI indices calculated on the GEE platform. The second section discusses the drought condition with available drought monitoring indices in TerraClimate datasets, and in the last section, the various indices based on Landsat datasets on pre- and postmonsoon seasons are analyzed to quantify the variation on vegetation and climate through indices like NDVI, VHI, VCI, TCI, LST, and NDWI.

11.4.1 Distribution of precipitation over the time period

Precipitation plays a crucial role in the analysis of drought conditions. It is the primary source of water for agricultural activities, and any significant deviations in its patterns can lead to agricultural droughts. Understanding precipitation trends is therefore crucial for predicting and managing drought conditions. In this present study, the **TerraClimate** data was analyzed from January to December (Fig. 11.4A). We observed substantial fluctuations in precipitation, particularly in January, February, November, and December. During these months, some years had almost no precipitation, indicating potential periods of agricultural drought. The monthly detailed analysis is given below:

January: The average precipitation is **8.63 mm**. The standard deviation is high at **11.45 mm**, indicating the spread from **almost no rainfall** in many dry years (2003, 2006, 2007, 2011, 2018, and 2010) to a **33 mm** moderately wet outlier in 2012 (Fig. 11.5). Most Januarys (over two-thirds) see rainfall of 0−15 mm. However, the high variation poses farming challenges. **February**: The **13.14 mm** average precipitation also has substantial fluctuation between 0 mm droughts (2005, 2006, 2009) and a very wet 66 mm year (2019), with a standard deviation of **16.89 mm**. The majority of years record modest 0−15 mm rain, but extremes disrupt crop planning. **March**: The **18.85 mm** average includes a huge 0−64 mm swing between extreme dry and wet Marches. With a **16.55 mm** standard deviation, most years see rainfall group between 15 and 30 mm. However, unpredictable large shifts in moisture early in the growing season complicate decisions. **April**: Despite averaging **45.63 mm** precipitation, April has varied enormously between basically none up to a flooded 150 mm (2020) due to a high **34.24 mm** standard deviation. Most Aprils receive 25−100 mm, but such

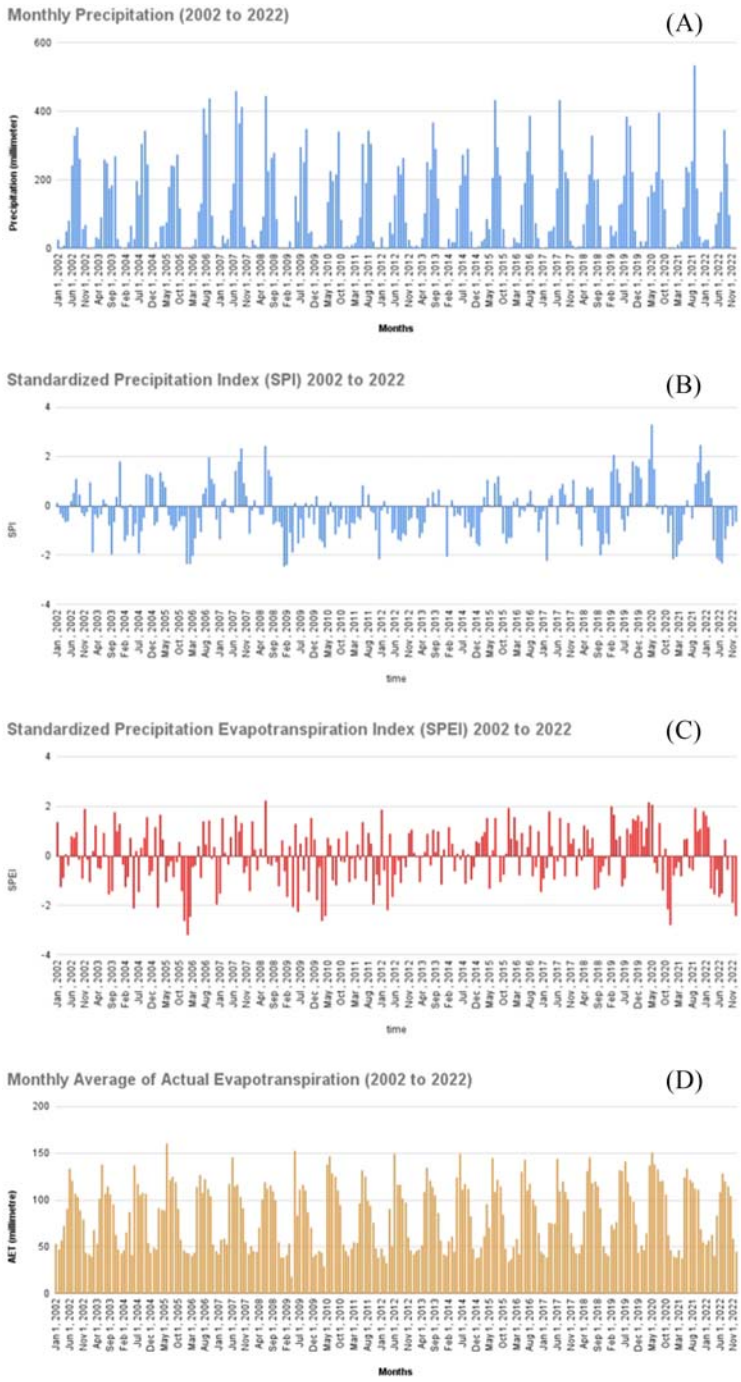

FIGURE 11.4

Timeseries for (A) Precipitation, (B) Standardized Precipitation Index, (C) Standardized Precipitation Evapotranspiration Index and (D) Actual Evapotranspiration from 2002 to 2022.

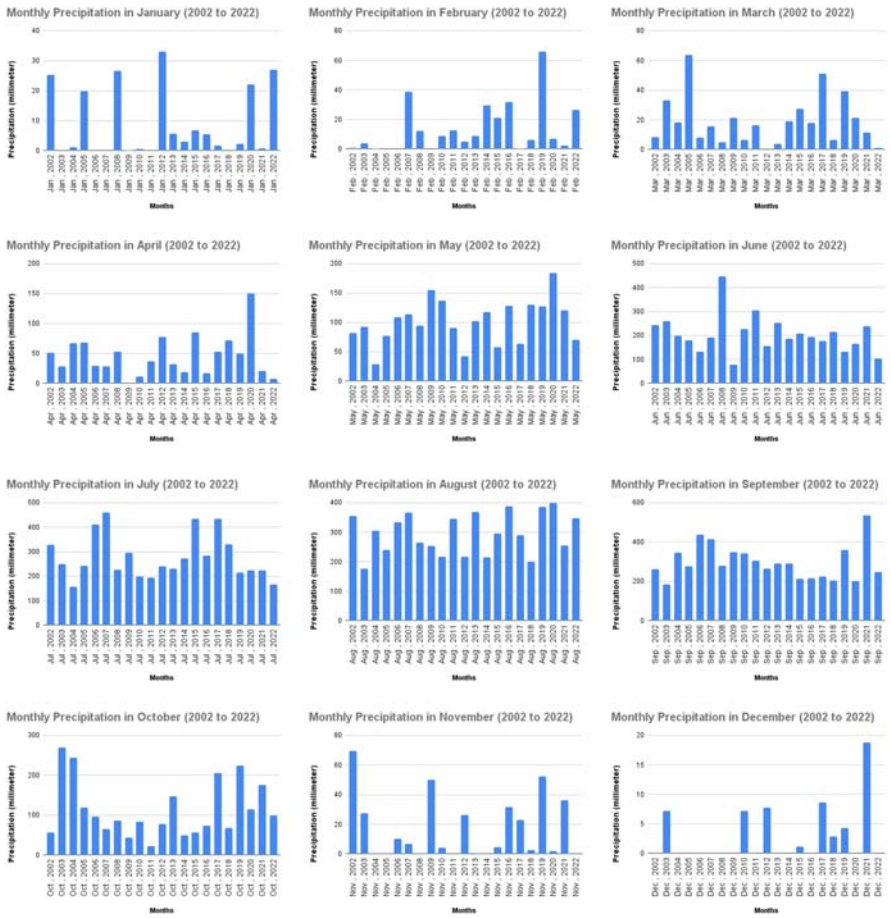

FIGURE 11.5

Monthly precipitation from 2002 to 2022.

volatility hampers crop growth. **May**: The **101.17 mm** average precipitation extends from 29 mm (2004) to over double that in very wet Mays. With a **37.56 mm** standard deviation, farmers must prepare both for half or double the benchmarks. Total rain of 50−150 mm is typical. **June**: Although averaging **204.24 mm**, June drenching swings wildly from just 78 mm (2009) to almost triple that due to a **77.37 mm** standard deviation. Most Junes average 125−300 mm. Planning amidst such variance is demanding.

July: Despite averaging in a hot **277.14 mm**, July precipitation has reached just 156 mm or over triple, reflecting its **90.35** mm standard deviation. Most rainfall is spread across a damp 200−400 mm historically. However, sensitivity is acute. **August**: The **295.87 mm** precipitation average sees volatility between just 176 mm

to nearly double with a **69.93** mm standard deviation. Most Augusts cluster within 200−375 mm. However, reliability is tough with shifts from damp to soaked conditions. **September**: The average precipitation is **297.05 mm**, but its **88.14 mm** standard deviation means it fluctuates between 185 and 533 mm. Most years see 200−375 mm total moisture. Yet early monsoons or extended dry periods pressurize farmers. **October**: Its **113.31 mm** precipitation mean ranges between just 22 and 269 mm, thanks to its **70.74 mm** standard deviation. Most rainfall is 50−200 mm. However, such instability right before harvests is problematic. **November**: Despite averaging **16.51 mm** precipitation, its **20.98 mm** standard deviation means many Novembers record zero rain, while the wet outlier saw nearly 70 mm. Most years cluster around 0−25 mm. However, moisture before the winter freeze is precious. **December**: With just **2.76 mm** average precipitation, Decembers tend to be bone dry with negligible **4.79 mm** standard deviation. Most see no moisture as winter sets in. Yet an 18 mm outlier poses challenges calculating frost and snow loads.

11.4.2 Temporal pattern of Standardized Precipitation Index and Standardized Precipitation Evapotranspiration Index

The SPI is a critical tool in the analysis of drought conditions. It operates on various timescales, making it a versatile index for drought monitoring. On shorter timescales, the SPI is closely tied to soil moisture levels, providing insights into **immediate drought conditions**. On longer timescales, it relates to groundwater and reservoir storage, offering a broader view of water availability. The SPI quantifies anomalies in accumulated precipitation over a specified period (e.g., 1, 3, and 12 months), making it an effective indicator for detecting and characterizing the onset, intensity, and duration of meteorological droughts (Dimyati et al., 2024). In this present study, the 1 month SPI was calculated to identify drought conditions. The time series given below represents the monthly SPI value from January 2002 to December 2022 (Fig. 11.4B). The precipitation dataset was used from the TerraClimate dataset for this analysis. Overall, the SPI value was positive in most months of the years 2005, 2007, 2019, 2021, and so forth and negative in most months of the years 2004, 2005. 2006, 2009, 2012, 2014. 2017, and 2022. The detailed monthly explanation is given in the next part.

The SPEI builds upon the SPI by incorporating PET into its calculations. This inclusion of PET allows the SPEI to account for the effects of temperature variability on drought conditions, in addition to precipitation. Therefore, the **SPEI provides a more comprehensive understanding of drought conditions** as it considers both water supply (precipitation) and demand (evapotranspiration). Like the SPI, the SPEI can also measure the severity of drought according to its intensity and duration and can identify the onset and end of drought episodes. In this study, 1 months SPEI was calculated to identify potential months with drought conditions.

Overall, the time series represents the drought condition from 2002 to 2022 (Fig. 11.4C). In the following months, the extreme positive SPEI was found,

indicating flood or wet conditions (June 2008, April 2020, May 2020, February 2019, December 2015, September 2021, November 2002, January 2012, and December 2021). Extreme negative means dry conditions were found in the months of January 2006, December 2020, March 2010, December 2005, February 2006, April 2010, December 2022, June 2009, March 2012, November 2020, May 2004, February 2005, and April 2009. The detailed Monthly explanation is given below.

January: In January, the years with the driest conditions were 2006, 2009, and 2014, indicating severe drought with significantly less than median precipitation. The wettest years were 2003, 2020, and 2022, which experienced higher than normal precipitation signaling very wet conditions. The year's closest to normal with SPI and SPEI values near the median were 2002, 2004, and 2013 (Fig. 11.6).

February: For February, the driest years were 2006, 2009, and 2017, with very low SPI and SPEI values pointing to extreme droughts. On the other hand, 2007, 2016, and 2019 were the wettest years, with high index values showing greater than average precipitation. February in the years 2008, 2014, and 2020 saw near median precipitation and normal conditions.

March: In terms of March, the years facing severe droughts and markedly less than normal rains were 2006, 2010, and 2012 based on the very low SPI and SPEI numbers. The opposite very wet years were 2005, 2017, and 2019 when the indices rose considerably beyond the median. Median levels aligning with normal precipitation were registered in 2008, 2014, and 2020.

April: April in 2009, 2010, and 2022 represented years of intense drought and the lowest SPI and SPEI readings. There was higher than typical precipitation in 2005, 2015, and 2020, the wettest years. 2004, 2007, and 2018 exhibited near normal April precipitation patterns and index numbers.

May: May 2004, 2012, and 2022 had dramatically less than normal rains pointing squarely toward severe droughts. Excess precipitation well beyond the median happened in 2005, 2019, and 2020, the wettest years. Normal median levels appeared in 2014, 2015, and 2016 for May (Fig. 11.6).

June: In June, acute dryness linked to rainfall shortages prevailed in 2009, 2012, and 2022, as seen through low SPI and SPEI metrics. The years 2008, 2011, and 2020 were instead the wettest owing to copious above average June showers. Normal precipitation similar to the median occurred in the years 2014, 2015, and 2016 (Fig. 11.6).

July: In July, the years facing severe drought with less than normal rains were 2004, 2012, and 2022 based on very low SPI and SPEI values. The opposite very wet years were 2007, 2008, and 2015, which saw higher than typical precipitation. Somewhere in between, with median July precipitation, were the years 2003, 2013, and 2016.

August: For August, acute dry spells linked to low rainfall happened in 2004, 2010, and 2012, as evident from the low index numbers. Excessive precipitation characterized 2002, 2007, and 2020, the wettest years. Normal August rainfall aligning with median index values occurred in 2020, 2018, and 2014.

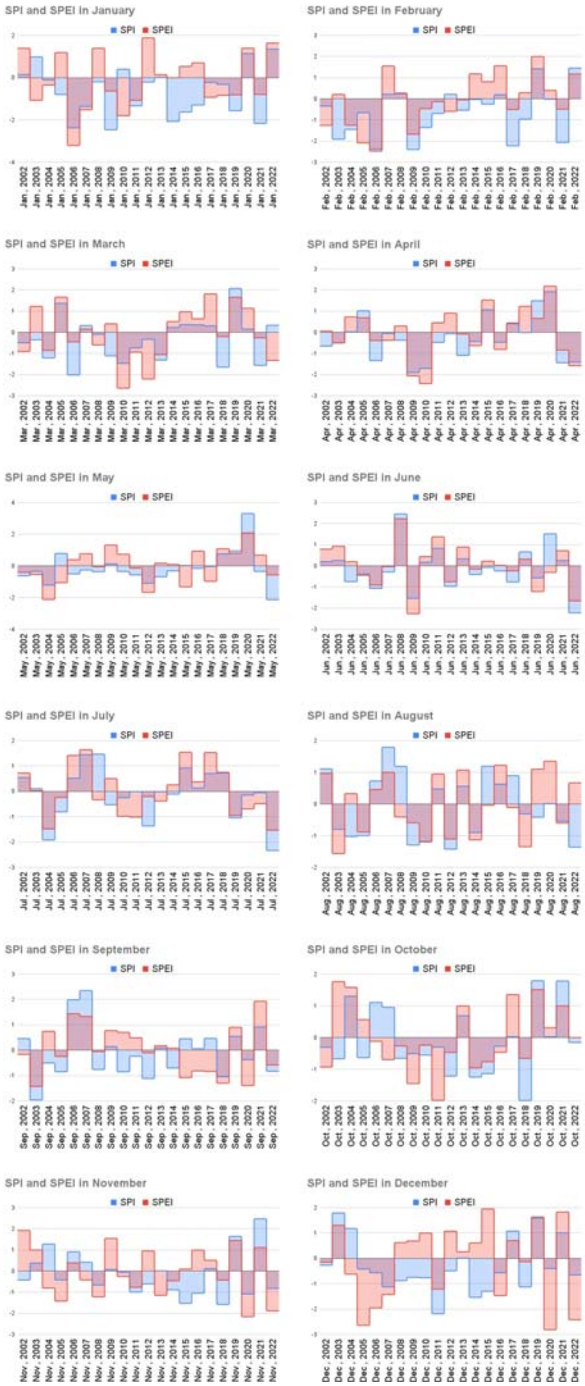

FIGURE 11.6

Monthly Standardized Precipitation Index (SPI) and Standardized Precipitation Evapotranspiration Index (SPEI) form 2002 to 2022.

September: September 2003, 2012, and 2022 faced extreme drought conditions owing to significantly less than average rains according to the SPI and SPEI. In contrast, the years 2006, 2007, and 2021 were very wet with ample above normal September showers. Near media precipitation fell in 2013, 2014, and 2016.

October; In October 2009, 2011, and 2018, SPI and SPEI metrics pointed strongly to intense droughts. The opposite situation of excess rainfall marked 2004, 2006, and 2019 as the wettest years. Normal precipitation similar to median levels happened in 2016, 2020, and 2022.

November: For November, 2005, 2015, and 2022 were the driest years as large rainfall deficiencies led to acute drought scenarios based on very low index numbers. 2002, 2006, and 2021 instead had the highest precipitation, classifying them as the wettest years. Average rainfall consistent with normal November patterns occurred in 2010, 2013, and 2017.

December: December 2011, 2014, and 2022 experienced severely dry conditions, with SPI and SPEI values indicating significant lack of precipitation. The wettest Decembers were 2003, 2019, and 2021 with rain surplus driving index values upward. Near media levels signifying normal rainfall prevailed in 2002, 2013, and 2018.

11.4.3 Distribution of actual evapotranspiration over the time

AET: It represents the actual amount of water that is evaporated and transpired, which is crucial for understanding water deficits during times of precipitation deficits. Fig. 11.4D shows monthly AET values in millimeters from January 2002 to December 2022. Over this two decades, AET levels followed a seasonal pattern, with the highest levels occurring during the summer months of June, July, and August and the lowest levels in the winter months of December, January, and February. Overall, June had the peak monthly AET averages over 130 mm in most years, exceedingly even 150 mm in some summers. In contrast, December and January AET averages were typically below 45 mm. The data indicates strong variability from year to year as well, with some years seeing relatively high evapotranspiration (e.g., the summer of 2020), while other years had lower levels (e.g., the low AET in the spring of 2009). There does not appear to be an obvious long-term trend up or down in average monthly AET over the time period. Instead, monthly AET seems to fluctuate considerably between years while retaining a consistent seasonal cycle peaking in mid-summer.

11.4.4 Distribution of climate water deficit over the time

It estimates how much additional water plants need. When water deficit is outside the normal range of plant adaptations, it restricts plant growth and other ecological processes. Fig. 11.7A shows monthly climate water deficit values in millimeters from January 2002 to December 2022. Deficit refers to the lack of water compared to the needs of plants. Over the two decades, deficit

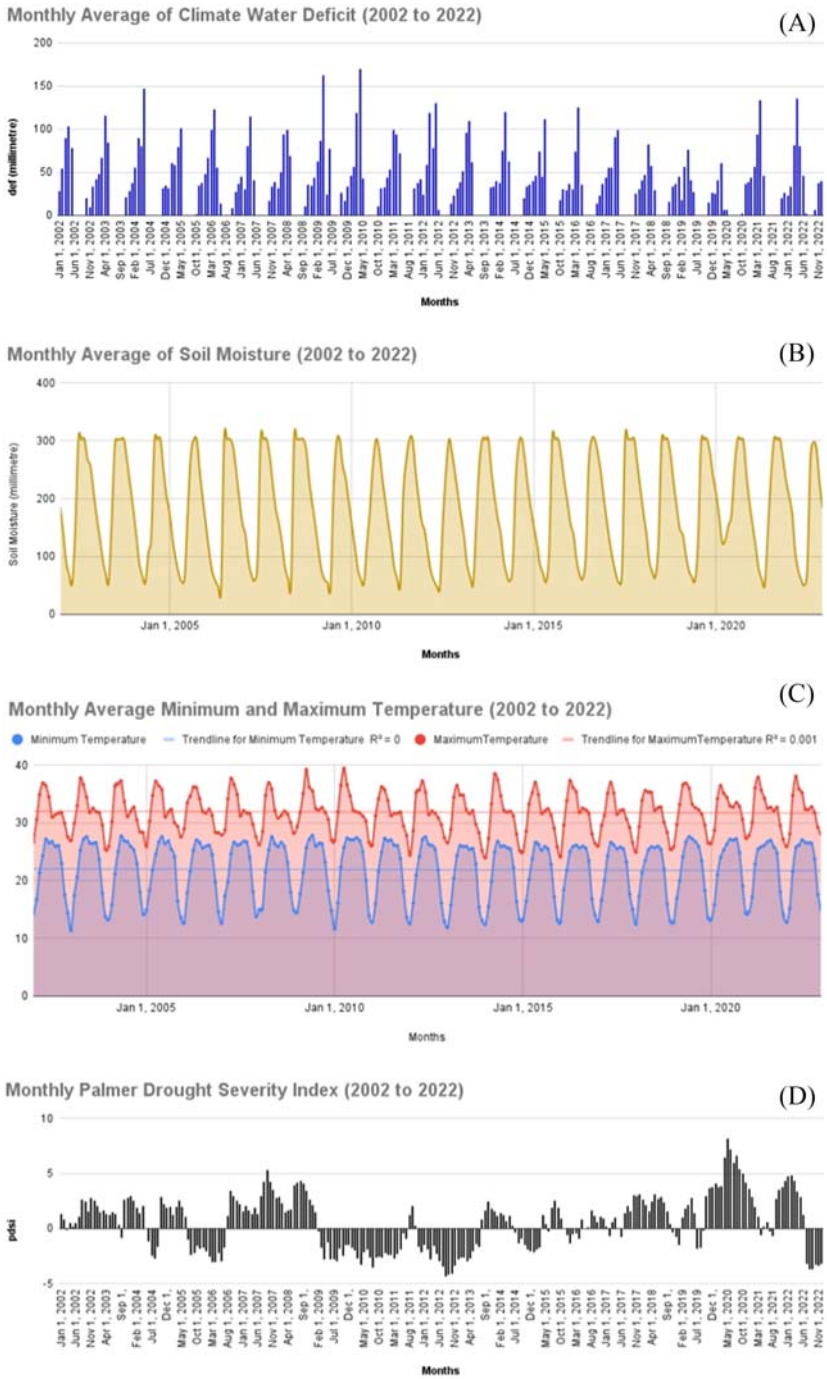

FIGURE 11.7

Timeseries for (A) Crop Water Deficit, (B) Soil Moisture, (C) Temperature, and (D) Palmer Drought Severity Index from 2002 to 2022.

followed a consistent seasonal pattern, with zero deficit occurring during the peak growing season in the summer months of June, July, and August when water demand is highest. During the winter months of December, January, and February, deficit levels were typically highest, exceeding 30 mm in most years. This reflects the lower water needs of plants in winter. The data shows considerable variability between years as well. Some years experienced prolonged zero deficits spanning spring and fall (e.g., 2003), while other years saw deficits persisting into the late spring and reemerging in early fall (e.g., 2009). The highest deficits appeared in the transitional seasons when water demand was rising or falling. There is no evident long-term trend over the 21-year period. Instead, monthly climate water deficit fluctuates year-to-year, while retaining a distinct seasonal cycle marked by zero summer deficit and peaks in the winter.

11.4.5 Distribution of soil moisture

Soil moisture: Reduced soil water levels are typically associated with soil water stress for vegetation, which constitutes a major constraint on the physiological functioning of natural and cultivated ecosystems and can thus lead to large impacts on agricultural production. Fig. 11.7B shows monthly soil moisture values in millimeters in the top 1 m of soil from January 2002 to December 2022. Over the 21-year record, soil moisture followed a consistent seasonal cycle, with the lowest levels occurring during the summer growing season and the highest moisture levels in the winter. June, July, and August showed very consistent soil moisture around 300 mm in most years, indicating field capacity conditions where the soil is fully saturated. In contrast, soil moisture declined sharply in the spring, reaching a low of around 50 mm on average in May just before the start of summer. Between years, soil moisture shows large variability during the transitional seasons, with some years retaining higher moisture later into spring (e.g., 2009), while other years dry down faster (e.g., 2004). On average, the data indicates a typical seasonal fluctuation between fully saturated winter soil moisture levels around 300 mm declining to roughly 50 mm just prior to summer, before rewetting in the fall. There is no obvious multiyear trend over the 21-year period. Rather, monthly soil moisture appears to vary year-to-year while retaining a distinct annual cycle.

11.4.6 Distribution of minimum and maximum temperature

They are important for understanding the thermal conditions of an area, which can influence evapotranspiration rates and thus the availability of water.

11.4.6.1 Minimum temperatures

The monthly minimum temperature data shows the lowest near-surface air temperatures in degrees Celsius from January 2002 to December 2022 (Fig. 11.7C).

Over this period, minimum temperatures followed a consistent seasonal cycle, reaching their lowest levels during winter months. The winter months of December, January, and February saw average minimums of 12°C−15°C. Minimum temperatures then steadily increased into the spring and summer months, typically peaking in July and August around 25°C−27°C. There was, however, considerable year-to-year variability in seasonal minimums overlaid on this pattern. Some years saw unusually cold winter minimums under 12°C, while other years had relatively warm winter lows of 15°C or greater. Overall there was no clear long-term trend toward warmer or colder minimum temperatures over the 21-year record. Rather, monthly minimum temperatures varied from year to year, while retaining a distinct seasonal cycle with winter lows and summer peaks.

11.4.6.2 Maximum temperatures

The monthly maximum temperature data shows the highest near-surface air temperatures in degrees Celsius over the same 2002−22 period. These maximum temperatures revealed a similar seasonal pattern as the minimums, with the hottest temperatures occurring during the summer and the coolest in the winter. On average, maximum temperatures peaked in the summer months of June, July, and August around 35°C−37°C. In contrast, winter maximum temperatures dropped to seasonal lows averaging around 25°C−28°C in December, January, and February (Fig. 11.7C). As with the minimums, however, substantial year-to-year variability is evident in the data. Some years saw significantly hotter summers or cooler winters. Overall, there is no clear long-term warming or cooling trend in maximum temperatures over the 21-year record when averaged on a monthly basis. Instead, monthly maximum temperatures appear to shift up and down year-to-year around a consistent seasonal cycle with summer peaks and winter troughs.

11.4.7 Distribution of Palmer Drought Severity Index over the study period

It is widely used for drought calculation and has the advantage of representing the actual drought characteristics while considering land and vegetation variability.

The PDSI data provides a measurement of relative drought and moisture conditions over the period from January 2002 to December 2022 (Fig. 11.7D). The index ranges from extreme drought indicated by large negative values to very wet moist periods shown by large positive values. Over the 21-year record, PDSI followed a fluctuating pattern, with some extended droughts punctuated by very moist wet spells. The most severe drought stretch occurred during the 2006−12 period, when PDSI remained almost continuously negative, dropping below −4

at times to indicate extreme drought. In contrast, brief wet periods emerged in some years like 2008–09 and 2019–20 when PDSI rose above +4. There was also large variability from month-to-month overlaid on multiyear wet/dry cycles. On average, late spring through early fall months appeared to be more prone to drought, while late fall into winter was climatologically wetter. However, seasonal impacts were modulated by variability on interannual scales. Overall, there was no clear long-term trend toward progressively drier or wetter conditions based on monthly PDSI over the period of record.

11.4.8 Correlation of drought indices

The provided correlation matrix displays relationships between nine drought indices (Fig. 11.8). The SPEI has strong positive correlations with several indices, indicating similar directional movements. There are also moderate and

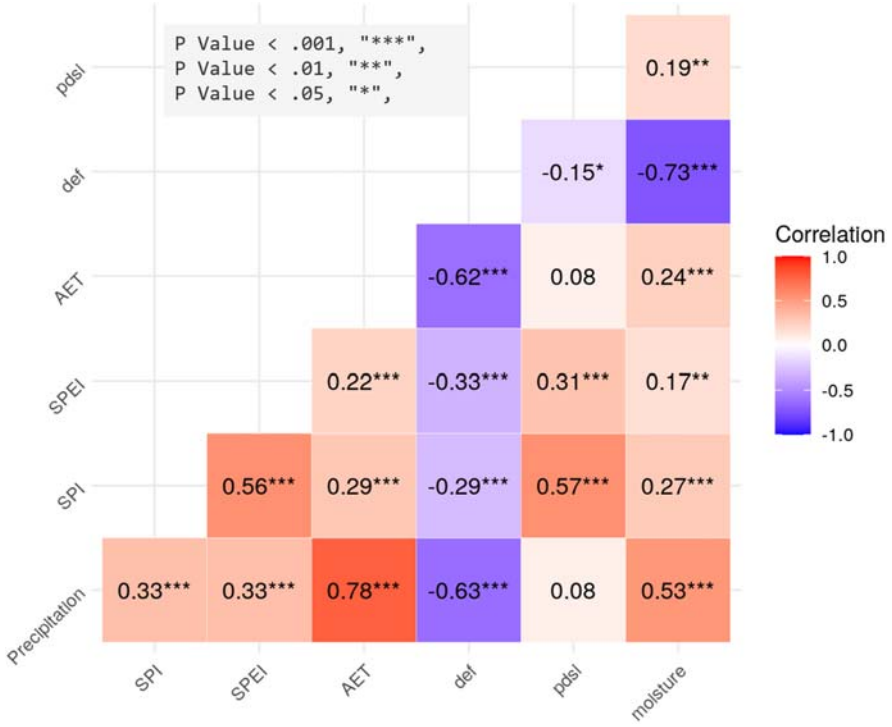

FIGURE 11.8

Correlation between drought indices.

weak correlations among other indices. Notably, as SPEI increases, the climate water deficit decreases, showing a negative correlation. The matrix's color coding visually represents these correlations, with asterisks indicating statistical significance. This matrix aids in understanding complex relationships between drought indices, informing drought risk assessments and management strategies. It emphasizes SPEI as a comprehensive drought measure but also indicates the need for a multiindex approach in drought analysis due to varying correlations with SPEI.

11.4.9 Impacts assessment of drought condition through different indices

Multiple satellite-based environmental indices are studied to understand agricultural drought patterns and farming potential in the region over 2002 to 2022 in the 5-year interval. The greenness, moisture stress, and temperature levels before and after monsoon are evaluated using indicators like NDVI, VHI, NDWI, LST, VCI, and TCI. Their trends showcase the climate-related challenges for regional agriculture as well as emerging resilience capacities. Steadily rising NDVI, NDWI, and VCI denote lowering crop moisture deficits over time. Cooling peak summertime temperatures are also positive for farming. Detailed analysis about the indicators is given below in Table 11.2.

11.4.9.1 Normalized Difference Vegetation Index

The NDVI values showed steady positive trends signaling gradual improvements in agricultural landscape health over the timeframes (Fig. 11.9). Premonsoon NDVI which reflects moisture adequacy for crops in the lead up to rains rose from 0.39 in 2003–07 to 0.57 in 2018–22. Postmonsoon NDVI, an indicator of rainwater utilization potential and agricultural productivity, increased from 0.51 to 0.62 over the same periods (Fig. 11.9). The rising cropland photosynthetic activity indicates progressive enhancements in vegetation condition and moisture availability despite climate risks. Possible factors enabling effective agricultural drought mitigation could be favorable shifts in precipitation patterns, expanded irrigation infrastructure, uptake of water conservation technologies, as well as cultivation of heat/drought resilient varieties.

11.4.9.2 Normalized Difference Water Index

The postmonsoon NDWI showed a transition from negative figures indicating agricultural droughts and moisture stress in early years to positive values in recent periods denoting adequate water content in croplands (Fig. 11.10). The NDWI rise from −0.42 in 2003–07 to 0.25 in 2018–22 after rains indicates wetter vegetation, improved rainwater retention in agricultural soils, and better hydrological

Table 11.2 Average of indices during pre- and postmonsoon over the time intervals.

Mean	2003–07 Pre	2003–07 Post	2008–12 Pre	2008–12 Post	2013–17 Pre	2013–17 Post	2018–22 Pre	2018–22 Post
NDVI	0.39	0.51	0.52	0.53	0.52	0.54	0.57	0.62
NDWI	−0.42	−0.49	−0.50	−0.45	−0.45	0.19	0.12	0.25
LST (°C)	31.13	29.78	30.72	30.08	31.10	30.29	30.98	30.26
VCI	0.46	0.55	0.68	0.73	0.51	0.53	0.55	0.56
TCI	0.51	0.42	0.48	0.41	0.52	0.46	0.54	0.57
VHI	0.48	0.49	0.58	0.57	0.52	0.49	0.54	0.56

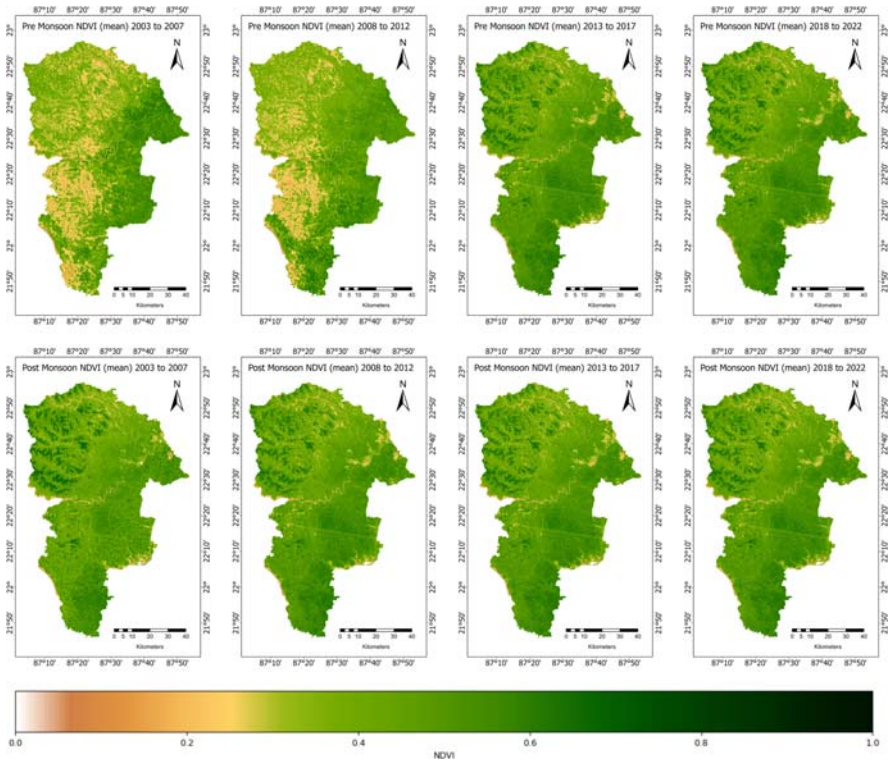

FIGURE 11.9

Normalized Difference Vegetation Index (NDVI) in pre- and postmonsoon.

accessibility for crops after the monsoon season (Fig. 11.10). This signals that the core monsoonal climate is now more effective in replenishing soil moisture and supporting agriculture in regions prone to moisture deficits. Contributing factors could include favorable spatial-temporal rainfall variations, adoption of soil/water conservation techniques, as well as expansion in the irrigated area enabled by groundwater access. Relief from higher evapotranspiration demands owing to tempering peak warming also plays a role.

11.4.9.3 Vegetation Condition Index

The VCI, indicating agricultural moisture stress and heat damage, showed consistent rising trajectories both before and after monsoons over the assessment time frames. Premonsoon VCI rose from 0.46 in 2003–07 to 0.55 in 2018–22. Postmonsoon VCI increased further from 0.55 to 0.56 (Fig. 11.11). The steady

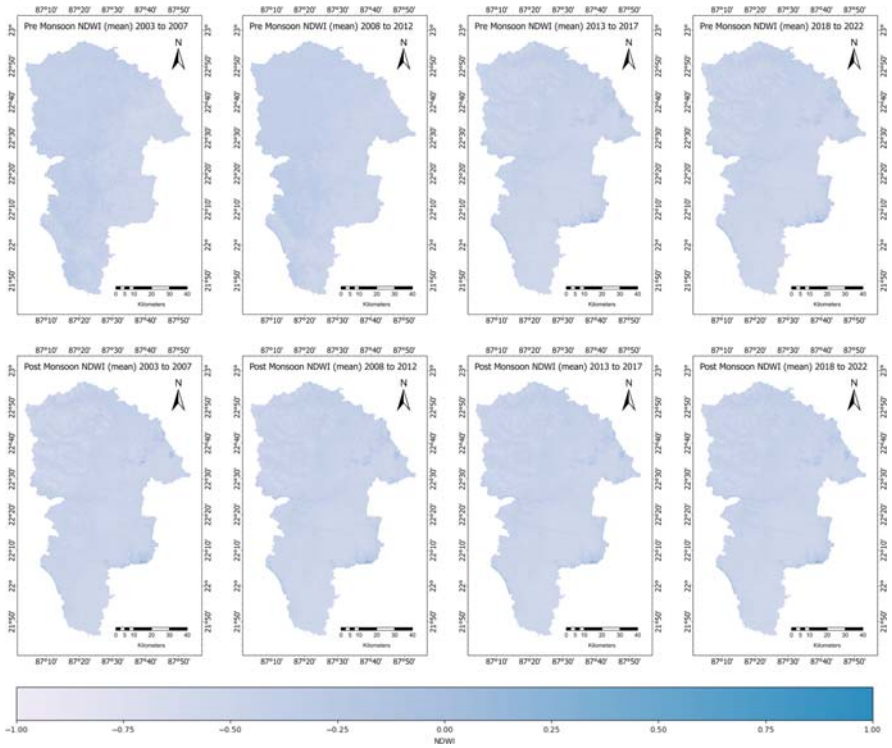

FIGURE 11.10

Normalized Difference Water Index (NDWI) in pre- and postmonsoon.

trends denote progressively lower moisture deficits and warming impacts on regional croplands in recent periods. Possible reasons include enhanced rainwater conservation in soils, expansion of irrigation infrastructure, shift toward heat resilient crop varieties, and so forth alongside the overarching rainfall improvements. Tempering of peak temperatures also plays a key role in alleviating farm-level climate risks. Marginally higher postmonsoon VCI signals effective utilization of monsoonal precipitation for agriculture. More importantly, narrowing gaps between pre- and postmonsoon VCI showcase strengthened capabilities of croplands to maintain robust health during drier periods.

11.4.9.4 Temperature Condition Index

\The postmonsoon TCI demonstrated a progressive increasing trend, rising from 0.42 to 0.57 over the assessment time periods (Fig. 11.12). This direction aligns with the cooling peak temperature patterns, indicating that agricultural landscape thermal

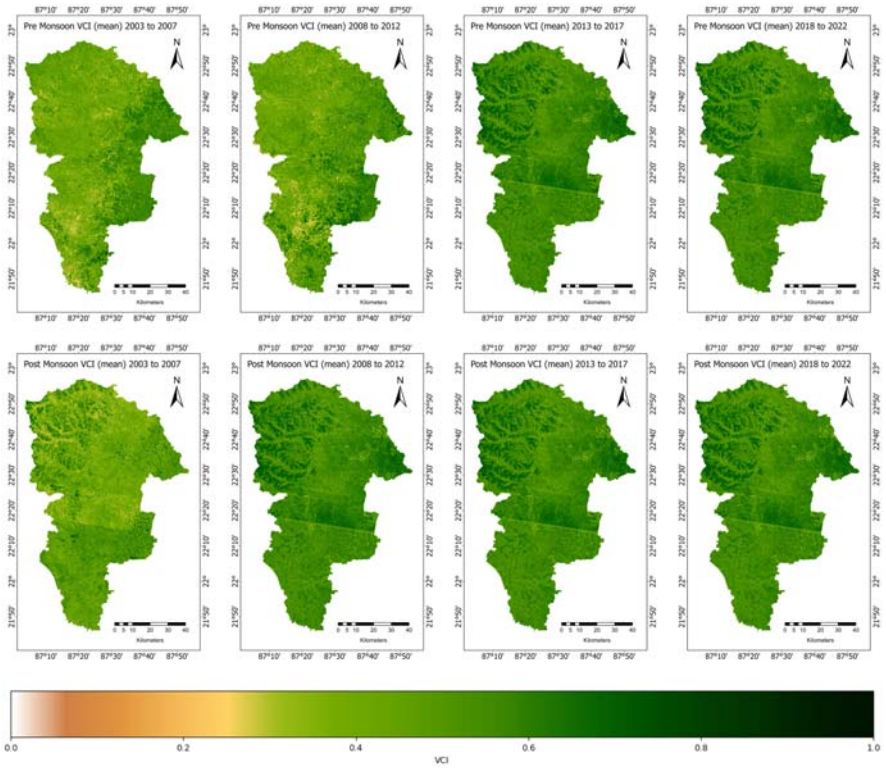

FIGURE 11.11

Vegetation Condition Index (VCI) in pre- and postmonsoon.

dynamics are turning more conducive, especially after rains. However, premonsoon TCI shows interyear fluctuations rather than any distinct trend. This points toward variability in heat extremes building up to the monsoon, a persisting area of concern for regional farming. Yet, the postmonsoon TCI gains showcase agriculture's enhanced capacities to offset periodic heat spikes in the lead up to rains by capitalizing on subsequent cooler temperatures after precipitation. Strengthening moisture retention abilities during rainy months also buffer premonsoon stresses.

11.4.9.5 Vegetation Health Index

The postmonsoon VHI fluctuated within a narrow band between 0.49 and 0.57 over the period (Fig. 11.13). This relative stability indicates average agricultural landscape health after monsoons, with typical vegetation conditions during the main cropping season neither improving drastically nor deteriorating markedly.

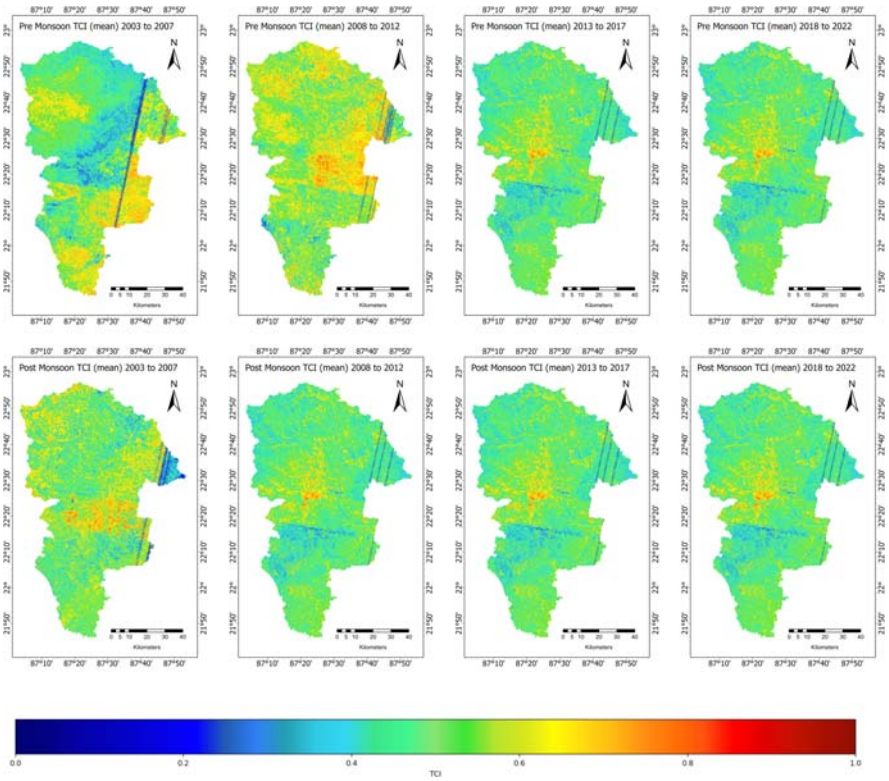

FIGURE 11.12

Temperature Condition Index (TCI) in pre- and postmonsoon.

However, the underlying contributors, viz., VCI and TCI showed independent positive movements when analyzed separately. The rising VCI denotes lowering crop moisture stress, while the TCI indicates relieving heat extremes, both conducive factors for rain-fed agriculture. Although balanced out in the aggregated VHI, these trends point toward reduced environmental constraints and expanded production potential. The steady VHI trajectory aligns with and substantiates the observed individual VCI and TCI shifts. In summation, typical postmonsoon VHI reassures stable cropland health outcomes, enabled by emerging warmth and soil moisture sufficiency that help counteract climate risks after rains.

11.4.9.6 Land surface temperature

The postmonsoon LST demonstrated a cooling trend over the time periods, dropping from 31.13°C in 2003–07 down to 30.26°C in 2018–22 (Fig. 11.14).

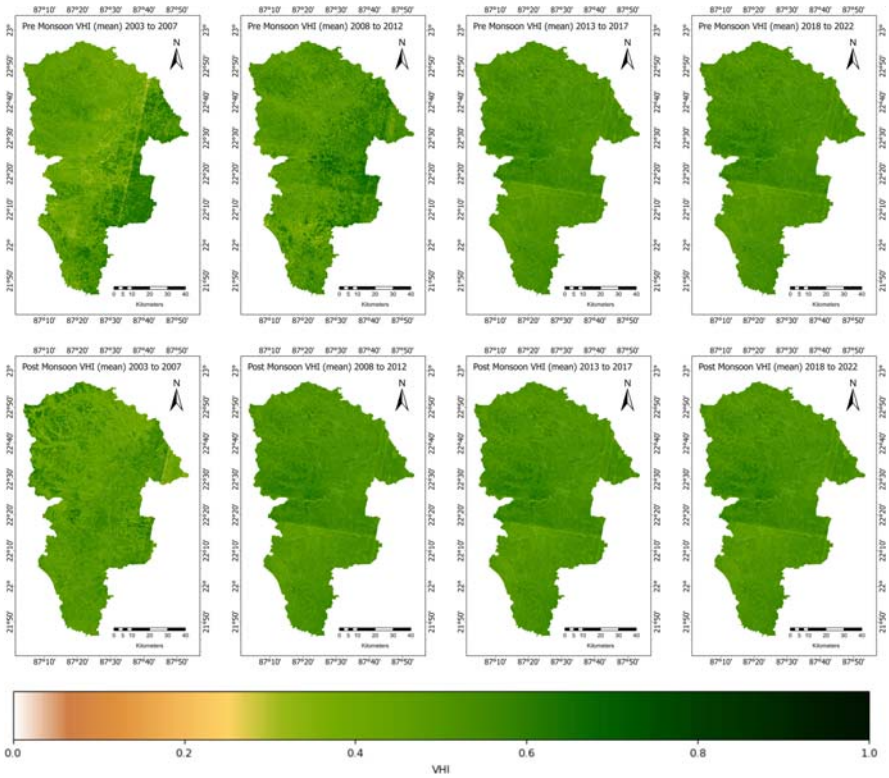

FIGURE 11.13

Vegetation Health Index (VHI) in pre- and postmonsoon.

This near 1°C fall in peak summertime warmth has favorable impacts for regional agriculture. Lower temperatures reduce evaporative moisture losses from soils and crops, preserving soil hydration in rain-fed croplands. Cooler peaks also minimize exposure to heat extremes during flowering and fruiting—critical crop growth stages vulnerable to warming. Together with the NDWI, reduced agricultural LST signifies stabilized hydrological cycling. Although premonsoon heat variability persists, the postmonsoon cooling enables crops to offset periodic stresses. It allows rainfall to translate into more effective moisture gains. Lower thermal extremes coupled with soil hydration maintenance ensure reduced agricultural drought risks. Consequently, heat stress-related farm income losses are averted, while also expanding regional climate resilience.

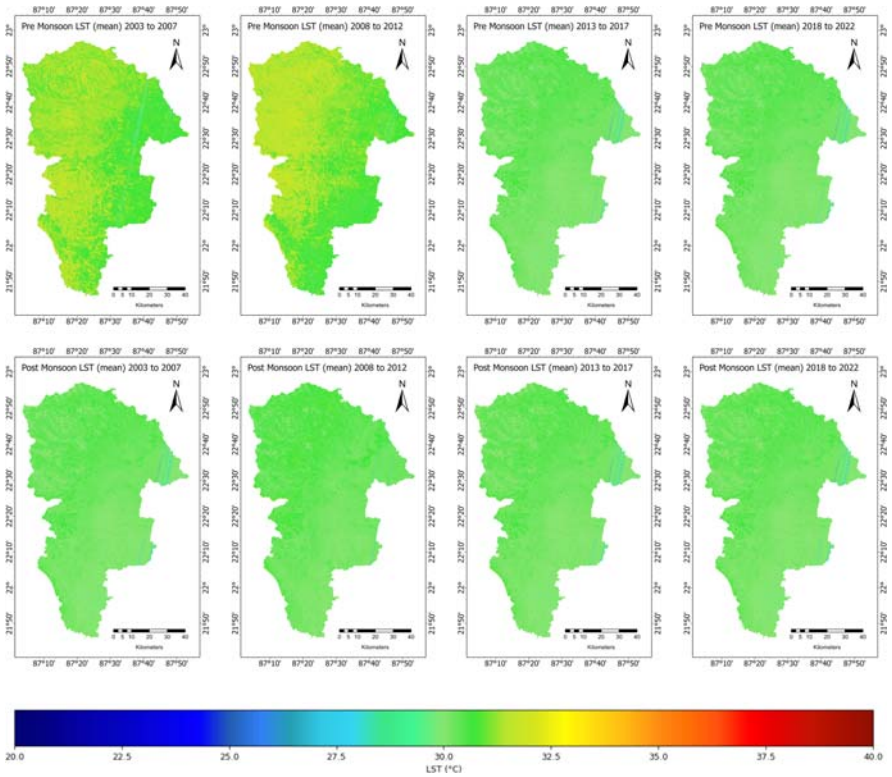

FIGURE 11.14

Land Surface Temperature (LST) in pre- and postmonsoon.

11.5 Conclusions

The analysis of Paschim Medinipur's agricultural drought patterns reveals several crucial conclusions regarding the region's climate risks and emergence of resilience. Precipitation is hugely variable, fluctuating wildly across years, seasons, and even months. Although the summer monsoon from June to September brings the bulk of annual rainfall, deviations from average norms are very common. This uncertainty around the quantity and timing of moisture availability leaves regional agriculture highly vulnerable to frequent drought occurrences, especially during critical crop establishment and harvesting periods. Multiple satellite-derived drought indicators confirm the prevalence of intense dry spells when below normal rains coincide with excessive heat. The years 2004, 2006, and 2009–12 experienced particularly devastating agricultural droughts as evidenced by extremely

low values in SPI, SPEI, and PDSI metrics coupled with vegetation moisture stress. Crop yields and harvested area shrunk drastically during these acute events, which also triggered substantial distress migration. In contrast, brief intervening periods like 2008–09 and selective years in the early 2010s and 2020 offered relative moisture sufficiency, pointing to multiyear cycling between opposite extremes. Responses in key vegetation indices like NDVI and VCI also trace these precipitation fluctuations, with moisture adequacy supporting productive croplands, while deficits severely impair crop conditions and farming livelihoods. However, overlaid on this precipitation variability are early indications that regional agriculture is developing capacities to better cope with and offset climatic uncertainty. The gradual long-term rises observed in postmonsoon NDVI, NDWI, and VCI denote enhanced vegetation health, soil moisture levels, and lowering crop water deficits in recent years aided by expanding irrigation infrastructure. Sizeable areas have adopted microirrigation and other water saving techniques. The concurrent cooling of peak summertime temperatures further alleviates heat extremes during critical flowering and yield formation stages. Together, these synergistic developments are equipping farms to capitalize on periodic wet spells, while withstanding frequent dry periods. In summary, while climate risks continue to disrupt Paschim Medinipur's rain-dependent agriculture, strategic interventions supporting emerging moisture conservation capacities can protect and enhance rural livelihoods. The momentum toward resilience evident through remote sensing indicators needs focused investments into adaptive irrigation techniques, heat-tolerant varieties, and associated ecosystem-based farm solutions to help decisively overcome precipitation variability. This will enable regional food and economic security imperatives to be sustainably achieved despite inevitable climate uncertainty ahead.

Acknowledgment

The authors extend their gratitude to the USGS and University of California Merced for providing free data and to Google Earth Engine for their complimentary computational resources. Your support has been invaluable to our study.

Appendix

1. Results tables: https://docs.google.com/spreadsheets/d/1Zl2l486Uir09cyGme40RmutAwJhskAcYwn0hic4OyXM/edit?usp = sharing
2. Google Earth Engine Scripts:
   a. Landsat 5: https://code.earthengine.google.com/8c01e98cc86dfd0a183c1e3cc293174f

b. Landsat 8: https://code.earthengine.google.com/e58c5bc76fcf57ad3cb27ca9ee61a160
c. SPI: https://code.earthengine.google.com/aa4eebe621c1173afb5c22425cb7c015
d. SPEI: https://code.earthengine.google.com/7a125e4c51b66219527b01a026e7231f
e. TerraClimate Timeseries: https://code.earthengine.google.com/50cb4631f068cd742f8eb105b14d84b5

References

Alahacoon, N., Edirisinghe, M., & Ranagalage, M. (2021). Satellite-based meteorological and agricultural drought monitoring for agricultural sustainability in Sri Lanka. *Sustainability*, *13*(6). Available from https://doi.org/10.3390/su13063427.

Amin, M., Khan, M. R., Hassan, S. S., Khan, A. A., Imran, M., Goheer, M. A., … Perveen, A. (2020). Monitoring agricultural drought using geospatial techniques: A case study of thal region of Punjab, Pakistan. *Journal of Water and Climate Change*, *11*(1S), 203−216. Available from https://doi.org/10.2166/wcc.2020.232.

Anderson, M. C., Norman, J. M., Mecikalski, J. R., Otkin, J. A., & Kustas, W. P. (2007). A climatological study of evapotranspiration and moisture stress across the continental United States based on thermal remote sensing: 1. Model formulation. *Journal of Geophysical Research Atmospheres*, *112*(10). Available from https://doi.org/10.1029/2006JD007506, http://onlinelibrary.wiley.com/journal/10.1002/(ISSN)2169-8996.

Ara, S., Alif, M. A. U. J., & Islam, K. M. A. (2021). Impact of tourism on LULC and LST in a coastal island of Bangladesh: A geospatial approach on St. Martin's Island of Bay of Bengal. *Journal of the Indian Society of Remote Sensing*, *49*(10), 2329−2345. Available from https://doi.org/10.1007/s12524-021-01389-4, http://www.springerlink.com/content/0255-660X.

Becker-Reshef, I., Vermote, E., Lindeman, M., & Justice, C. (2010). A generalized regression-based model for forecasting winter wheat yields in Kansas and Ukraine using MODIS data. *Remote Sensing of Environment*, *114*(6), 1312−1323. Available from https://doi.org/10.1016/j.rse.2010.01.010.

Cai, S., Zuo, D., Wang, H., Han, Y., Xu, Z., Wang, G., & Yang, H. (2024). Improvement of drought assessment capability based on optimal weighting methods and a new threshold classification scheme. *Journal of Hydrology*, *631*, 130758. Available from https://doi.org/10.1016/j.jhydrol.2024.130758, https://www.sciencedirect.com/science/article/pii/S0022169424001525.

Cai, S., Zuo, D., Wang, H., Xu, Z., Wang, G. Q., & Yang, H. (2023). Assessment of agricultural drought based on multi-source remote sensing data in a major grain producing area of Northwest China. *Agricultural Water Management*, *278*. Available from https://doi.org/10.1016/j.agwat.2023.108142.

Chattopadhyay, N., Malathi, K., Tidke, N., Attri, S. D., & Ray, K. (2020). Monitoring agricultural drought using combined drought index in India. *Journal of Earth System Science*, *129*(1). Available from https://doi.org/10.1007/s12040-020-01417-w.

Dimyati, M., Rustanto, A., Shiddiq, I. P. A., Indratmoko, S., Siswanto., Dimyati, R. D., … Auni, R. (2024). Spatiotemporal relation of satellite-based meteorological to agricultural drought in the downstream Citarum watershed, Indonesia. *Environmental and Sustainability Indicators*, 100339. Available from https://doi.org/10.1016/j.indic.2024.100339, https://www.sciencedirect.com/science/article/pii/S2665972724000072.

Dong, H., Li, J., Yuan, Y., You, L., & Chen, C. (2017). A component-based system for agricultural drought monitoring by remote sensing. *PLoS One*, *12*(12). Available from https://doi.org/10.1371/journal.pone.0188687.

Dutta, D., Kundu, A., Patel, N. R., Saha, S. K., & Siddiqui, A. R. (2015). Assessment of agricultural drought in Rajasthan (India) using remote sensing derived Vegetation Condition Index (VCI) and Standardized Precipitation Index (SPI). *The Egyptian Journal of Remote Sensing and Space Science*, *18*(1), 53−63. Available from https://doi.org/10.1016/j.ejrs.2015.03.006.

Eklund, L., Mohr, B., & Dinc, P. (2024). Cropland abandonment in the context of drought, economic restructuring, and migration in northeast Syria. *Environmental Research Letters*, *19*(1). Available from https://doi.org/10.1088/1748-9326/ad1723.

Geng, G., Zhang, B., Gu, Q., He, Z., & Zheng, R. (2024). Drought propagation characteristics across China: Time, probability, and threshold. *Journal of Hydrology*, *631*, 130805. Available from https://doi.org/10.1016/j.jhydrol.2024.130805, https://www.sciencedirect.com/science/article/pii/S0022169424001999.

Ghaleb, F., Mario, M., & Sandra, A. N. (2015). Regional landsat-based drought monitoring from 1982 to 2014. *Climate*, *3*(3), 563−577. Available from https://doi.org/10.3390/cli3030563.

González, J., & Valdés, J. B. (2006). New drought frequency index: Definition and comparative performance analysis. *Water Resources Research*, *42*(11). Available from https://doi.org/10.1029/2005WR004308.

Gorelick, N., Hancher, M., Dixon, M., Ilyushchenko, S., Thau, D., & Moore, R. (2017). Google Earth Engine: Planetary-scale geospatial analysis for everyone. *Remote Sensing of Environment*, *202*, 18−27. Available from https://doi.org/10.1016/j.rse.2017.06.031.

Govind, N. R., & Ramesh, H. (2020). Exploring the relationship between LST and land cover of Bengaluru by concentric ring approach. *Environmental Monitoring and Assessment*, *192*(10). Available from https://doi.org/10.1007/s10661-020-08601-x, https://link.springer.com/journal/10661.

Hasan, I. F., & Abdullah, R. (2022). Agricultural drought characteristics analysis using copula. *Water Resources Management*, *36*(15), 5915−5930. Available from https://doi.org/10.1007/s11269-022-03331-w, https://www.springer.com/journal/11269.

Hazaymeh, K., & Hassan, Q. (2016). Remote sensing of agricultural drought monitoring: A state of art review. *AIMS Environmental Science*, *3*, 604−630. Available from https://doi.org/10.3934/environsci.2016.4.604.

Jana, A., Sit, G., & Chanda, A. (2021). Ichthyofaunal diversity of river Kapaleswari at Paschim Medinipur district of West Bengal, India. *Flora and Fauna*, *27*(1). Available from https://doi.org/10.33451/florafauna.v27i1pp113-124.

Ji, L., & Peters, A. J. (2003). Assessing vegetation response to drought in the northern Great Plains using vegetation and drought indices. *Remote Sensing of Environment*, *87*(1), 85−98. Available from https://doi.org/10.1016/S0034-4257(03)00174-3, http://www.elsevier.com/inca/publications/store/5/0/5/7/3/3.

Kaur, L., Rishi, M. S., & Chaudhary, B. S. (2022). Assessment of meteorological and agricultural droughts using remote sensing and their impact on groundwater in an agriculturally productive part of Northwest India. *Agricultural Water Management*, *274*. Available from https://doi.org/10.1016/j.agwat.2022.107956.

Kloos, S., Yuan, Y., Castelli, M., & Menzel, A. (2021). Agricultural drought detection with modis based vegetation health indices in southeast Germany. *Remote Sensing*, *13* (19). Available from https://doi.org/10.3390/rs13193907.

Kogan, F. N. (1995). Application of vegetation index and brightness temperature for drought detection. *Advances in Space Research*, *15*(11), 91−100. Available from https://doi.org/10.1016/0273-1177(95)00079-t.

Kumar, V., & Chu, H.-J. (2024). Seasonal drought severity identification using a modified multivariate index: a case study of Indo-Gangetic Plains in India. *Journal of Hydrology*, *629*. Available from https://doi.org/10.1016/j.jhydrol.2024.130632.

Liu, Y. Y., Parinussa, R. M., Dorigo, W. A., De Jeu, R. A. M., Wagner, W., Van Dijk, A. I. J. M., … Evans, J. P. (2011). Developing an improved soil moisture dataset by blending passive and active microwave satellite-based retrievals. *Hydrology and Earth System Sciences*, *15*(2), 425−436. Available from https://doi.org/10.5194/hess-15-425-2011.

Liu, X., Zhu, X., Pan, Y., Li, S., Liu, Y., & Ma, Y. (2016). Agricultural drought monitoring: Progress, challenges, and prospects. *Journal of Geographical Sciences*, *26*(6), 750−767. Available from https://doi.org/10.1007/s11442-016-1297-9.

Li, H., Yin, Y., Zhou, J., & Li, F. (2024). Improved agricultural drought monitoring with an Integrated Drought Condition Index in Xinjiang, China. *Water (Switzerland)*, *16*(2). Available from https://doi.org/10.3390/w16020325.

Mckee, T.B., Doesken, N.J., & Kleist, J. (1993). The relationship of drought frequency and duration to time scales. In *Eighth conference on applied climatology* (pp. 17−22).

Mishra, A. K., & Singh, V. P. (2010). A review of drought concepts. *Journal of Hydrology*, *391*(1−2), 202−216. Available from https://doi.org/10.1016/j.jhydrol.2010.07.012.

Mistry, P., & Suryanarayana, T. (2023). Assessment & monitoring of agricultural drought indices using remote sensing techniques and their inter-comparisonassessment & monitoring of agricultural drought indices using remote sensing techniques and their inter-comparison. *Ecological Perspective*, *3*, 1−8. Available from https://doi.org/10.53463/ecopers.20230171.

Moran, M. S., Clarke, T. R., Inoue, Y., & Vidal, A. (1994). Estimating crop water deficit using the relation between surface-air temperature and spectral vegetation index. *Remote Sensing of Environment*, *49*(3), 246−263. Available from https://doi.org/10.1016/0034-4257(94)90020-5.

Panda, K. P., Upadhyay, A., Jha, M. K., & Sharma, S. P. (2020). Mapping of laterite zones using 2D electrical resistivity tomography survey in parts of Paschim Medinipur, West Bengal, India: An approach for artificial groundwater recharge. *Journal of Earth System Science.*, *129*(1). Available from https://doi.org/10.1007/s12040-020-01390-4, https://rd.springer.com/journal/12040.

Pan, Y., Zhu, Y., Lü, H., Yagci, A. L., Fu, X., Liu, E., … Liu, R. (2023). Accuracy of agricultural drought indices and analysis of agricultural drought characteristics in China between 2000 and 2019. *Agricultural Water Management*, *283*. Available from https://doi.org/10.1016/j.agwat.2023.108305.

Possega, M., Ojeda, M. G.-V., & Gámiz-Fortis, S. R. (2023). Multi-scale analysis of agricultural drought propagation on the iberian peninsula using non-parametric indices. *Water (Switzerland)*, *15*(11). Available from https://doi.org/10.3390/w15112032.

Bashit, N., Ristianti, N. S., & Ulfiana, D. (2022). Drought assessment using remote sensing and geographic information systems (GIS) techniques (Case Study: Klaten Regency, Indonesia). *International Journal of Geoinformatics*, *18*(5), 115−127. Available from https://doi.org/10.52939/ijg.v18i5.2393.

Roy, S., Hazra, S., & Chanda, A. (2023). Assessment of wet season agricultural droughts using monthly MODIS and SAR data in the red and lateritic zone of West Bengal, India. *Spatial Information Research*, *31*(2), 195−210. Available from https://doi.org/10.1007/s41324-022-00485-y.

Senamaw, A., Addisu, S., & Suryabhagavan, K. V. (2021). Mapping the spatial and temporal variation of agricultural and meteorological drought using geospatial techniques, Ethiopia. *Environmental Systems Research*, *10*(1). Available from https://doi.org/10.1186/s40068-020-00204-2.

Senapati, U., Raha, S., Das, T. K., & Gayen, S. K. (2021). *A composite assessment of agricultural drought susceptibility using analytic hierarchy process: Case study of western region of West Bengal*. *Agriculture, food and nutrition security: A study of availability and sustainability in India* (pp. 15−40). Springer International Publishing, https://link.springer.com/book/10.1007/978-3-030-69333-6. doi: 10.1007/978-3-030-69333-6_2.

Sen, U. K., & Bhakat, R. (2021). Quantitative evaluation of biological spectrum and phenological pattern of vegetation of a sacred grove of West Midnapore District, Eastern India. *Asian Journal of Forestry.*, *5*, 83−100. Available from https://doi.org/10.13057/asianjfor/r050206.

Seshasai, M., Murthy, C., Chandrasekar, K., Jeyaseelan, A., Diwakar, P., & Dadhwal, V. (2016). Agricultural drought: Assessment & monitoirng. *Mausam*, *67*. Available from https://doi.org/10.54302/mausam.v67i1.1155.

Shahfahad, M., Rihan, M. W., Naikoo, M. A., Ali, T. M., & Usmani, A. R. (2021). Urban heat island dynamics in response to land-use/land-cover change in the Coastal City of Mumbai. *Journal of the Indian Society of Remote Sensing*, *49*(9), 2227−2247. Available from https://doi.org/10.1007/s12524-021-01394-7, http://www.springerlink.com/content/0255-660X.

Sims, A. P., Niyogi, D. D. S., & Raman, S. (2002). Adopting drought indices for estimating soil moisture: A North Carolina case study. *Geophysical Research Letters*, *29*(8). Available from https://doi.org/10.1029/2001GL013343, http://onlinelibrary.wiley.com/journal/10.1002/(ISSN)1944-8007/issues?year = 2012.

Sreekesh, S., Kaur, N., & Naik, S.S. R. (2019). Agricultural drought and soil moisture analysis using satellite image based indices. In *International archives of the photogrammetry, remote sensing and spatial information sciences − ISPRS archives* (pp. 507−514). International Society for Photogrammetry and Remote Sensing India. http://www.isprs.org/proceedings/XXXVIII/4-W15/ 16821750 3 42 10.5194/isprs-archives-XLII-3-W6-507-2019.

Sruthi, S., & Mohammed Aslam, M.A. (2015). Agricultural drought analysis using the NDVI and land surface temperature data; a case study of Raichur District. In *International conference on water resources, coastal and ocean engineering (ICWRCOE'15)* (vol. 4, pp. 1258−1264). 2214-241X. https://www.sciencedirect.com/science/article/pii/S2214241X15001650. doi: 10.1016/j.aqpro.2015.02.164.

Tanarhte, M., De Vries, A. J., Zittis, G., & Chfadi, T. (2024). Severe droughts in North Africa: A review of drivers, impacts and management. *Earth-Science Reviews*, *250*, 104701. Available from https://doi.org/10.1016/j.earscirev.2024.104701, https://www.sciencedirect.com/science/article/pii/S001282522400028X.

Thavorntam, W., & Tantemsapya, N. (2013). Vegetation greenness modeling in response to climate change for Northeast Thailand. *Journal of Geographical Sciences*, *23*(6), 1052−1068. Available from https://doi.org/10.1007/s11442-013-1062-2.

Tran, T. V., Bruce, D., Huang, C.-Y., Tran, D. X., Myint, S. W., & Nguyen, D. B. (2023). Decadal assessment of agricultural drought in the context of land use land cover change using MODIS multivariate spectral index time-series data. *GIScience and Remote Sensing*, *60*(1). Available from https://doi.org/10.1080/15481603.2022.2163070.

Vicente-Serrano, S. M., Beguería, S., & López-Moreno, J. I. (2010). A multiscalar drought index sensitive to global warming: The standardized precipitation evapotranspiration index. *Journal of Climate*, *23*(7), 1696−1718. Available from https://doi.org/10.1175/2009JCLI2909.1Spain, http://journals.ametsoc.org/doi/pdf/10.1175/2009JCLI2909.1.

Wang, S., Chu, H., Gong, C., Wang, P., Wu, F., & Zhao, C. (2022). The effects of COVID-19 lockdown on air pollutant concentrations across China: A Google Earth Engine-based analysis. *International Journal of Environmental Research and Public Health*, *19*(24). Available from https://doi.org/10.3390/ijerph192417056.

Xiao, X., Ming, W., Luo, X., Yang, L., Li, M., Yang, P., … Li, Y. (2024). Leveraging multisource data for accurate agricultural drought monitoring: A hybrid deep learning model. *Agricultural Water Management*, *293*. Available from https://doi.org/10.1016/j.agwat.2024.108692, https://doi.org/10.1016/j.agwat.2024.108692.

Zhang, Z., Guo, H., Feng, K., Wang, F., Zhang, W., & Liu, J. (2024). Analysis of agricultural drought evolution characteristics and driving factors in Inner Mongolia inland river basin based on three-dimensional recognition. *Water*, *16*(3). Available from https://doi.org/10.3390/w16030440, 2073-4441.

Zhang, L., Huang, W., & Li, S. (2024). Multivariate time series convolutional neural networks for long-term agricultural drought prediction under global warming. *Agricultural Water Management*, *292*. Available from https://doi.org/10.1016/j.agwat.2024.108683, https://doi.org/10.1016/j.agwat.2024.108683.

Zhang, Y., Wu, Z., Singh, V. P., Jin, J., Zhou, Y., Xu, S., & Li, L. (2022). Agricultural drought assessment in a typical plain region based on coupled hydrology−crop growth model and remote sensing data. *Remote Sensing*, *14*(23). Available from https://doi.org/10.3390/rs14235994.